MNRAS 000, 1–20 (2021) Preprint 26 July 2021 Compiled using MNRAS LATEX style file v3.0

Radio Continuum Sources behind the Large Magellanic Cloud

M. D. Filipović,[1]★ I. S. Bojičić,[1] K. R. Grieve,[1] R. P. Norris,[1,2] N. F. H. Tothill,[1] D. Shobhana,[1] L. Rudnick,[3] I. Prandoni,[4] H. Andernach,[5] N. Hurley-Walker,[6] R. Z. E. Alsaberi,[1] C. S. Anderson,[2] J. D. Collier,[1,7] E. J. Crawford,[1] B.-Q. For,[7,8] T. J. Galvin,[6] F. Haberl,[10] A. M. Hopkins,[11,1] A. Ingallinera[12] P. J. Kavanagh,[13] B. S. Koribalski,[1,2] R. Kothes,[14] D. Leahy,[15] H. Leverenz,[1] P. Maggi,[16] C. Maitra,[10] J. Marvil,[17] T. G. Pannuti,[18] L. A. F. Park,[1] J. L. Payne,[1] C. M. Pennock,[19] S. Riggi,[12] G. Rowell,[20] H. Sano,[21] M. Sasaki,[22] L. Staveley-Smith,[7,8] V. Trigilio,[12] G. Umana,[12] D. Urošević,[23,24] J. Th. van Loon,[19] E. Vardoulaki,[25]

[1]*Western Sydney University, Locked Bag 1797, Penrith South DC, NSW 2751, Australia*
[2]*CSIRO Astronomy and Space Science, PO Box 76, Epping, NSW 1710, Australia*
[3]*Minnesota Institute for Astrophysics, School of Physics and Astronomy, University of Minnesota, 116 Church Street SE, Minneapolis, MN 55455, USA*
[4]*INAF – Istituto di Radioastronomia, Via P. Gobetti 101, 40129, Bologna, Italy*
[5]*Depto. de Astronomía, DCNE, Universidad de Guanajuato, Cjón. de Jalisco s/n, Col. Valenciana, Guanajuato, CP 36023, Gto., Mexico*
[6]*International Centre for Radio Astronomy Research, Curtin University, Bentley, WA 6102, Australia*
[7]*The Inter-University Institute for Data Intensive Astronomy (IDIA), Department of Astronomy, University of Cape Town, Rondebosch 7701, South Africa*
[8]*ARC Centre of Excellence for All Sky Astrophysics in 3 Dimensions (ASTRO 3D), Australia*
[9]*International Centre for Radio Astronomy Research, University of Western Australia, 35 Stirling Hwy, Crawley, WA 6009, Australia*
[10]*Max-Planck-Institut für extraterrestrische Physik, Gießenbachstraße 1, D-85748 Garching, Germany*
[11]*Australian Astronomical Optics, AAO-Macquarie, Faculty of Science and Engineering, Macquarie University, 105 Delhi Rd, North Ryde, NSW 2113, Australia*
[12]*INAF – Osservatorio Astrofisico di Catania, via Santa Sofia 78, I-95123 Catania, Italia*
[13]*School of Cosmic Physics, Dublin Institute for Advanced Studies, 31 Fitzwilliam Place, Dublin 2, Ireland*
[14]*Dominion Radio Astrophysical Observatory, Herzberg Astronomy and Astrophysics, National Research Council Canada, PO Box 248, Penticton BC V2A 6J9, Canada*
[15]*Department of Physics and Astronomy, University of Calgary, University of Calgary, Calgary, Alberta, T2N 1N4, Canada*
[16]*Observatoire Astronomique de Strasbourg, Université de Strasbourg, CNRS, 11 rue de l'Université, F-67000 Strasbourg, France*
[17]*National Radio Astronomy Observatory, 1003 Lopezville Road, Socorro, NM 87801, USA*
[18]*Department of Physics, Earth Science and Space Systems Engineering, Morehead State University, 235 Martindale Drive, Morehead, KY 40351, USA*
[19]*Lennard-Jones Laboratories, Keele University, Staffordshire ST5 5BG, UK*
[20]*School of Physical Sciences, The University of Adelaide, Adelaide 5005, Australia*
[21]*National Astronomical Observatory of Japan, Mitaka, Tokyo 181-8588, Japan*
[22]*Remeis Observatory and ECAP, Universität Erlangen-Nürnberg, Sternwartstraße 7, D-96049 Bamberg, Germany*
[23]*Department of Astronomy, Faculty of Mathematics, University of Belgrade, Studentski trg 16, 11000 Belgrade, Serbia*
[24]*Isaac Newton Institute of Chile, Yugoslavia Branch*
[25]*Thüringer Landessternwarte, Sternwarte 5, 07778 Tautenburg, Germany*

Accepted 2021 July 22. Received 2021 July 22; in original form 2021 March 18

ABSTRACT

We present a comprehensive multi-frequency catalogue of radio sources behind the Large Magellanic Cloud (LMC) between 0.2 and 20 GHz, gathered from a combination of new and legacy radio continuum surveys. This catalogue covers an area of ∼144 deg^2 at angular resolutions from 45 arcsec to ∼3 arcmin. We find 6 434 discrete radio sources in total, of which 3 789 are detected at two or more radio frequencies. We estimate the median spectral index (α; where $S_\nu \sim \nu^\alpha$) of $\alpha = -0.89$ and mean of -0.88 ± 0.48 for 3 636 sources detected exclusively at two frequencies (0.843 and 1.384 GHz) with similar resolution (Full Width at Half-Maximum (FWHM) ∼40–45 arcsec). The large frequency range of the surveys makes it an effective tool to investigate Gigahertz Peak Spectrum (GPS), Compact Steep Spectrum (CSS) and Infrared Faint Radio sources populations within our sample. We find 10 GPS candidates with peak frequencies near 5 GHz, from which we estimate their linear size. 1 866 sources from our catalogue are CSS candidates with $\alpha < -0.8$. We found six candidates for High Frequency Peaker (HFP) sources, whose radio fluxes peak above 5 GHz and no sources with unconstrained peaks and $\alpha > 0.5$. We found optical counterparts for 343 of the radio continuum sources, of which 128 have a redshift measurement. Finally, we investigate the population of 123 Infrared Faint Radio Sources (IFRSs) found in this study.

Key words: Magellanic Clouds – radio continuum: general – galaxies: active – catalogues

1 INTRODUCTION

Various peoples of the southern hemisphere, including Australian Aborigines, incorporated the Magellanic Clouds (MCs) as an important part of their culture. These obvious astronomical objects of the southern sky were seen by Portuguese explorer Ferdinand Magellan in the 16th century. He described the MCs as the most vivid celestial objects of the southern sky seen during his mesmerising expeditions (for more details on historical observations of MCs see: Filipovic et al. 1996a).

The LMC is thought to be a barred spiral galaxy, dynamically disrupted due to its proximity to the Milky Way (MW) and other interactions with the Small Magellanic Cloud (SMC) (Mathewson et al. 1974). The LMC is currently ~50 kpc (Pietrzyński et al. 2013, 2019; Riess et al. 2019) from the centre of the MW, while the SMC is further away at a distance of ~60 kpc (Hilditch et al. 2005). In addition, this well-known distance and motion of the LMC allows for accurate calculations of the total energy that has been released from Supernova Remnants (SNRs) (Maggi et al. 2016; Bozzetto et al. 2017; Maggi et al. 2019; Leahy et al. 2019; Yew et al. 2021). A detailed optical study of 715 LMC Planetary Nebulae (PNe) is presented by Reid & Parker (2013) and Reid (2014). To date, 31 of these objects have been detected at radio wavelengths by Payne et al. (2008), Filipović et al. (2009), Vukotić et al. (2009) and Leverenz et al. (2017) with 28 having a complete radio-surface-brightness-to-diameter ($\sum - D$) relation derived from 6 cm surveys. Each of these objects have been observed at multiple radio wavelengths from 3 to 20 cm. Since the LMC is seen almost face-on from the MW, it is a perfect laboratory for studying complete populations with accurate energy measurements (Riess et al. 2019).

The last few decades have seen extensive multi-frequency surveys of the sky in the direction of these two galaxies, primarily investigating objects within the MCs themselves. These various surveys present a prime opportunity to study not just intrinsic Magellanic Cloud (MC) objects but also a large population of background active galactic nuclei (AGN) and quasars located in the sky area around the LMC. This massive collection of data allows for a high level analysis of the AGN population with reasonable spectral resolution, sensitivity and spatial resolution.

Large scale radio continuum surveys by Filipovic et al. (1996b, 1998a,b) allowed for a detailed overview of H II and star forming regions intrinsic to the MCs. 469 discrete sources in the direction of the LMC were detected using the Parkes telescope between 1.4 and 8.55 GHz (Filipovic et al. 1995). Of these, 209 have been classified as H II regions or SNRs. This analysis has allowed for a detailed understanding of the overall structure of the LMC and SMC. Additionally, the detection of these objects allowed cross identification with infrared surveys to investigate the radio–to–infrared comparison (Filipovic et al. 1998c). Most recently, For et al. (2018), presented a survey of the MCs using a low-frequency wideband telescope, the Murchison Widefield Array (Wayth et al. 2015).

Large background source catalogues have a twofold significance: **1)** they enable population studies to understand the evolution of radio objects and by – extension – the evolution of the Universe, and **2)** they allow for the study of foreground media, through Faraday rotation imparted on polarised sources. These Faraday rotation measurements further improve the understanding of the magnetic field strength and direction as measured by Haynes et al. (1991). Building on this, Gaensler et al. (2005); Mao et al. (2012); Kaczmarek et al. (2017) utilised these background catalogues to more accurately determine the magnetic field strength within the LMC.

From this wealth of data, combined with new surveys and observations, we can further understand the evolution and composition of the AGN population. In this paper, we describe the process of source finding and cross-matching these various source lists to construct a large catalogue of radio sources in the direction of the LMC. We examine each source to determine its radios properties. Our new catalogue presented here is best compared and similar to the Australia Telescope Large Area Survey (ATLAS; at 1400 MHz Norris et al. 2006; Middelberg et al. 2008) that covered a total of ~6 deg^2 on the sky, down to a Root Mean Squared (rms) noise level of <30 μJy. The ATLAS survey uncovered over 3 000 distinct radio sources out to a redshift of 2. Our similar resolution and increased sky coverage will serve to significantly increase our knowledge of these distant objects.

2 OBSERVATIONAL DATA

We have used a number of radio continuum images from archival data to detect discrete sources in the direction of the LMC. These data have been taken with the Murchison Widefield Array (MWA), Australian Square Kilometre Array Pathfinder (ASKAP), the Molonglo Observatory Synthesis Telescope (MOST) and the Australia Telescope Compact Array (ATCA) telescopes (details are shown in Table 1). These observations were originally used to detect and categorise sources and regions intrinsic to the LMC. Below, we describe each of the data sets that we used in this study.

2.1 MWA Images

Low-frequency surveys are becoming increasingly important in the understanding of objects such as young SNRs, CSS and GPS sources. In particular, this is important for GPS sources as the turnover can be more accurately identified at this end of the radio frequency bandwidth. As part of the GaLactic Extragalactic All-sky MWA (GLEAM) survey (Wayth et al. 2015), For et al. (2018) presented a series of selected images of the MCs. We used the 0.2 GHz (robust=−1) image, which has the lowest noise and best angular resolution for this study of individual sources (see Table 1).

2.2 ASKAP-Beta Image

In this paper, we present a new 0.843 GHz image from the Australian Square Kilometre Array Pathfinder (ASKAP) Telescope Boolardy Engineering Test Array (BETA) (Hotan et al. 2014) that covers a $9.5^\circ \times 9.8^\circ$ area of the LMC field. This observation was performed in 2015 May as an early ASKAP testing field with a bandwidth of 1 MHz. At this time, ASKAP was operated as a 6 antenna interferometer using first generation Phased Array Feed (PAF) receivers. Each receiver produced nine independent beams which were arranged on the sky as a 3×3 grid with a grid spacing of 1.46 degrees. The extent of the LMC was covered by mechanically re-pointing the antennas at four field centres to reposition the beam pattern on the sky. To increase the density of the mosaic pattern, an additional four field centres were observed, each of which was offset from the original field centre by 0.73 degrees in both RA and Dec (see Heywood et al. (2016) for a more detailed description).

The observations cycled through these 8 field centres approximately once per hour for 10 hours, producing the equivalent of a 72-pointing mosaic with a traditional, single-beam instrument. These data from each of the 72 beam/field combinations were processed independently using the ASKAPSoft software package and

pipeline. The bandpass and flux density were calibrated using a separate observation of PKS B1934−638. This source was observed at the centre of each of the 9 PAF beams, and calibrated against the Reynolds (1994) model. These data for each beam/field combination were then imaged and self-calibrated independently and the final images were merged into a linear mosaic. From this, we achieve an average rms noise level of 0.71 mJy beam^{-1} and a FWHM of 61 × 53 arcsec.

Note that our ASKAP-Beta image was made at a very early stage of the ASKAP testing. As expected, a range of issues such as positional accuracy, beam forming accuracy, and calibration were discovered. We have made every effort to identify and correct these problems. These efforts have subsequently contributed to understanding and improving the performance of ASKAP generally. As a result, a newer higher-sensitivity and resolution ASKAP survey at 888 MHz was recently produced (Pennock et al. 2021). This new survey is built upon results presented here.

2.3 MOST 0.843 GHz Image

To further enhance our frequency coverage of sources in the direction of the LMC, we use the 0.843 GHz image from the MOST using observations from 1981 that pre-dates the Sydney University Molonglo Sky Survey (SUMSS) (Sect. 2.6.2) as described by Mills & Turtle (1984). This image reaches a rms of between 0.3 and 0.6 mJy beam^{-1} with a resolution of 43 arcsec and a bandwidth of 3 MHz. This survey was initially constructed to maximise detection of SNRs and H II regions within the MCs. In this study, however, we decided to use only SUMSS as a core catalogue (also see Sect. 3.4.3) to be used for the source spectral index investigation as we found the MOST flux densities to be unreliable, especially for the fainter sources.

2.4 ATCA 1.384 GHz Image

Radio continuum emission at ∼1.4 GHz is produced from a variety of sources on all scales. Typically, the use of only one telescope (or array configuration) is not sufficient to fully sample all spatial scales. To counteract this, we have chosen to use the 1.384 GHz images from Hughes et al. (2006, 2007) and Payne et al. (2009) who combine the ATCA and Parkes telescopes LMC surveys (Haynes et al. 1991; Filipovic et al. 1995, 1996b, 1998b). The ATCA Telescope observations were undertaken with four different array configurations providing 40 unique baselines, with a maximum baseline of 750 m. This allows for high resolution observations to be combined with zero spacing (single-dish) data. Once combined, the final image has a FWHM of 40 arcsec with a rms of ∼0.5 mJy beam^{-1}. The data from these two telescopes were taken between 1994 and 1996, covering a 10.8° × 12.3° area. This field fully covers the LMC with sufficient room beyond the extent of the diffuse emission of the LMC, allowing for a detailed study of various source types to be undertaken.

2.5 ATCA 4.8 and 8.64 GHz Images

Dickel et al. (2005) observed the LMC using the ATCA's dual band observing mode; one 128 MHz band was placed at a central frequency of 8.64 GHz and the second at a central frequency of 4.8 GHz. The main science goal for this survey was to observe and identify SNRs and H II regions that reside within the LMC. These data were combined with observations made with the Parkes telescope (Haynes et al. 1991; Filipovic et al. 1995, 1996b, 1998b) to allow the broad, diffuse radio structure of the LMC to be analysed. 7085 separate ATCA pointing centres were used to cover the 6° × 6° area, with additional sampling around the 30 Doradus (30 Dor) region. With angular resolutions of 33 arcsec (at 4.8 GHz) and 20 arcsec (at 8.64 GHz), images were created to be sensitive to the target objects and at the same time closely matching the then-existing X-ray, optical and Infrared (IR) surveys. The resolution from the 352-m and 367-m arrays (configured by excluding the sixth antenna) presents an issue of poor resolution (>1 arcmin) so that sources could not easily be distinguished as background objects or objects within the LMC. From this, a rms sensitivity of 0.28 mJy beam^{-1} and 0.5 mJy beam^{-1} was achieved for the 4.8 and 8.64 GHz images, respectively.

2.6 Supplementary Surveys

We make use of an additional four radio surveys and five optical catalogues as summarised in Tables 1 and 2 respectively. These supplementary surveys allow for radio continuum spectra to be sampled over the range of 0.408 to 20 GHz, to detect sources with curved or peak radio spectra. Additionally, the inclusion of the SUMSS catalogue provides 0.843 GHz data for the full ATCA 1.384 GHz field. We further include optical surveys to obtain redshift measurements for a small subset of objects.

2.6.1 Molonglo Reference Catalogue of Radio Sources

The Molonglo Reference Catalogue of Radio Sources (MRC) (Large et al. 1981) was established using the MOST telescope between 1968 and 1974, detecting 12 141 sources brighter than 0.7 Jy at 408 MHz. This was achieved with a rms of 18 – 60 mJy beam^{-1}. The total survey area covers 7.85 sr (∼25770 degrees^2), with an overall source density of 1 500 sr^{-1} (∼0.456 per 1 degree^2). The catalogue is reasonably complete above ∼1 Jy, however, the flux measurements between 0.7 and 1 Jy may be unreliable.

2.6.2 The Sydney University Molonglo Sky Survey

The Sydney University Molonglo Sky Survey (SUMSS) (Bock et al. 1999; Mauch et al. 2003) was completed in 2007 using MOST and covering the Southern sky south of −30° with $|b| > \pm 10°$. This survey was designed as an extension of the NRAO VLA Sky Survey (NVSS) on the same grid and at a similar resolution. However, the SUMSS Survey observed at 0.843 GHz with a bandwidth of 3 MHz compared to the ∼ 50 MHz bandwidth of the 1.4 GHz NVSS survey. These two surveys, SUMSS and NVSS, overlap in the region –40<Dec< −30° and catalogues have been published that contain 210 412 and 1 773 484 sources, respectively (Condon et al. 2002; Mauch et al. 2008). While the rms noise level of SUMSS (∼1 mJy beam^{-1}) is about twice that of NVSS, the $u - v$ coverage for SUMSS is superior to NVSS, allowing for extended objects with lower surface brightness to be detected.

2.6.3 The Parkes-MIT-NRAO (PMN)

The Parkes-Massachusetts Institute of Technology (MIT)-National Radio Astronomy Observatory (NRAO) Survey of the sky South of Dec=+10° was performed in 1990 using the Parkes Radio Telescope outfitted with the NRAO seven beam receiver at 4.850 GHz (Griffith & Wright 1993) with FWHM of 252 arcsec. 36 640 sources across

the Southern sky were detected down to a 5σ level with a rms of >4.2 mJy beam^{-1}. As for the SUMSS, we make use of this catalogue but not of the images.

2.6.4 *The Australia Telescope 20 GHz Survey*

The Australia Telescope 20 GHz Survey (AT20G) is a blind survey that looks for objects above a given rms anywhere in the given sky patch. It was conducted at 19.904 GHz using a bandwidth of 248 MHz that surveyed the entire Southern sky at Dec< 0°. The primary objective was to categorise and analyse radio populations at high frequencies on an unprecedented scale. Murphy et al. (2010) have presented a catalogue of 5 890 sources detected at a flux density level of at least 40 mJy with a 91 per cent completeness above 100 mJy for declination south of −15°, and 79 per cent above 50 mJy beam^{-1} (some data were lost due to weather for declinations above −15°).

2.6.5 *6dF Galaxy Survey*

The 6dF Galaxy Survey (Jones et al. 2005a,b) is an optical survey conducted with the 1.2 m UK Schmidt Telescope with the goal of obtaining spectroscopy for a magnitude limited sample of galaxies to (K, H, J, r_F, b_J) = (12.75, 13.00, 13.75, 15.60, 16.75). This was achieved with the 6 degree Field (6dF) instrument, using 150 spectroscopic fibres positioned by a robot on the focal plane. From this, 136 304 redshifts of galaxies were measured for galactic latitudes $|b|$ >10 deg, over an area of 17 000 deg^2. Each source in the 6dF catalogue was selected from the Two Micron All Sky Survey Extended Source Catalogue (2MASX) catalogue (Jarrett et al. 2000; Skrutskie et al. 2006) (K_{tot} < 12.75). A near-infrared selection has a twofold effect: **1)** the target sample is less affected by dust extinction; **2)** typically, candidates selected solely through optical means will be dominated by young, blue stellar populations. However, candidates chosen through near-infrared criteria are dominated by their oldest population of stars, allowing for more robust galactic mass measurement, and are more likely to host an AGN.

2.6.6 *Magellanic Quasars Survey (MQS)*

Kozłowski & Kochanek (2009); Kozłowski et al. (2011, 2012, 2013) classified a total of 6 103 optical sources in the direction of the LMC as Quasi-Stellar Object (QSO)'s using Australian Astronomical Telescope (AAT). Of these sources, 962 have redshift measurements. Crucially, these sources were selected using multiple methods to confirm that they do not belong to the LMC. Each source was inspected for its mid-IR colours compared against existing optical surveys, with the Spitzer SAGE survey (Meixner et al. 2006) and the OGLE-III survey (Udalski et al. 1994). The redshift measurements presented in these surveys are of great importance as they allow us to disentangle sources within the LMC against the background AGN. Additionally, these surveys allow for the ease of cross-matching radio sources to the CatWISE2020 IR source catalogue (as shown in Sect. 2.6.8).

2.6.7 *MACHO Survey*

The MACHO survey, as presented by Kim et al. (2012), provides measurements of 663 QSO candidates in the direction of the LMC with the intent of searching for Massive Astrophysical Compact Halo Objects (MACHO). These sources were cross-matched with additional surveys, such as Spitzer SAGE, Two Micron All Sky Survey (2MASS), *Chandra*, the *XMM-Newton* and a LMC UBVI catalogs. The authors applied machine learning techniques to these data, allowing for a high confidence classification of each source. This gives an estimated false positive rate of 1 per cent for cross identification with other surveys. This allows us to identify sources in our radio catalogue with QSO candidates from Kim et al. (2012).

2.6.8 *CatWISE2020 Catalogue*

The Wide-Field Infrared Survey Explorer (WISE) space telescope has mapped the whole sky at wavelengths of 3.4, 4.6, 11.6 and 22 µm (hereafter W1, W2, W3 and W4) as presented by Wright et al. (2010). From this, the CatWISE2020 catalogue was created (Marocco et al. 2021) where all existing data products from all phases were combined to make the most sensitive all-sky mid-IR survey to date. In total, two complete and 10 additional all sky passes were made (data collected from 2010 to 2018), allowing for identification and rejection of asteroids and other solar system objects[1]. This survey was conducted until the telescope ran out of liquid helium, pushing the rms significantly higher than initially designed. Recently, Marocco et al. (2021) produced a catalogue of over 1 890 715 640 entries for the W1 and W2 bands.

3 RADIO SOURCE CATALOGUE

We generated five new source lists of discrete radio-continuum sources from the 0.843 (ASKAP-Beta), 0.843 (MOST), 1.384, 4.8 and 8.64 GHz ATCA images. When combined with the existing SUMSS, a total of 6 434 unique discrete radio sources have been detected in at least one of these catalogues. The source finding for each image was performed as a blind search without the use of prior knowledge from any existing catalogues.

Sources detected in these lists are a combination of sources belonging to the LMC (such as SNRs, H II regions or PNe) and background objects in the direction of the LMC. By cross-matching (radius of 10 arcsec) with objects in Simbad Database (Wenger et al. 2000), no known objects from our Galaxy were detected in any of the previous radio surveys of this area that we study here in this paper. Galactic radio sources are expected to have a low surface density in the direction of the LMC due to its high Galactic latitude (Filipovic et al. 1998b).

3.1 Source Finding and Cross-matching

The Aegean Source Finding suite of tools (Hancock et al. 2012a,b, 2018) have been used to process the core radio surveys, creating a catalogue of the sources within the field, including source positions, sizes and integrated flux densities. A two-step process was applied to the images for source detection, firstly forming a background and rms map, and subsequently running the source finding routine. The background and rms maps were created with The Background And Noise Estimation tool (Bane) using a moving box-car smoothing method. Using this rms map improves the integrity of the flood fill operation used in Aegean as it is able to more accurately determine the source extent, and thus the integrated flux density of the source. For both Aegean and Bane we set tuning parameters to their default

[1] http://wise2.ipac.caltech.edu/docs/release/neowise/neowise_2019_release_intro.html

Table 1. Radio continuum surveys of the LMC used in this work. Surveys flagged with an asterisk were used to create discrete sources catalogued (Table 3) and to estimate spectral index. † indicates that the field is restricted to the 1.384 GHz image size.

Survey	Telescope	Freq. (GHz)	Field Size (deg × deg)	rms (mJy beam^{-1})	Synthesised FWHM (″)	Mean Maj. & Min. Source Size (″)	Num. of Sources	Reference
GLEAM*	MWA	0.200	10.8 × 12.3†	17 – 20	162 × 139	171 × 146	1 277	This Work
MRC*	MOST	0.408	10.8 × 12.3†	18 – 60	156 × 172	N/A	40	Large et al. (1981)
SUMSS*	MOST	0.843	10.8 × 12.3†	∼1.2	45 × 47	54.27 × 46.98	3 636	Mauch et al. (2003)
ASKAP-Beta	ASKAP	0.843	9.5 × 9.8	0.71	61 × 53	66.81 × 56.73	1 995	This Work
MOST	MOST	0.843	7.7 × 7.9	0.30 – 0.40	45 × 47	48.90 × 44.19	2 084	This Work
ATCA*	ATCA	1.384	10.8 × 12.3	0.50	40	46.98 × 41.26	6 434	This Work
ATCA*	ATCA	4.80	6.0 × 6.3	0.28	33	40.97 × 34.89	570	This Work
PMN	Parkes	4.85	10.8 × 12.3†	∼8	252	312 × 254	191	Griffith & Wright (1993)
ATCA*	ATCA	8.64	6.0 × 6.3	0.50	20	25.64 × 21.70	279	This Work
AT20G*	ATCA	19.904	10.8 × 12.3†	∼10	13.9	N/A	38	Murphy et al. (2010)

Table 2. Optical surveys of the LMC used in this work.

Survey	Telescope	Unique Source Count	Matched Sources	Matched Sources with z	Reference
6dF	1.2-m UK Schmidt Telescope	540	111	84	Jones et al. (2009)
MACHO	50" Mt. Stromlo Telescope	3 407	31	27	Kim et al. (2012)
Magellanic Quasars Survey. I	Anglo-Australian Telescope	4 679	122	3	Kozłowski & Kochanek (2009)
Magellanic Quasars Survey. II	Anglo-Australian Telescope	677	10	0	Kozłowski et al. (2012)
Magellanic Quasars Survey. III	Anglo-Australian Telescope	565	20	20	Kozłowski et al. (2013)

values. The cross identification and visual analyses were performed with the Tool for OPerations on Catalogues And Tables (TOPCAT) (Taylor 2005, 2011) and SAOIMAGE DS9 (DS9) applications (Joye & Mandel 2003).

We used the following five steps to create the final source lists presented in this paper:

(i) Initially we began with a 5σ detection level, creating preliminary source lists from the 0.843 (ASKAP and MOST images), 1.384, 4.8 and 8.64 GHz images.

(ii) We manually examined sources that were close to S/N∼5 and $\theta_{major}/\theta_{minor} > 2$ to determine if they were spurious. Detections that were not genuine (e.g. due to imaging artefacts, or an increased noise level towards the field edge as evident in Figure 1) were flagged and removed.

(iii) We visually inspected large, extended sources belonging to the LMC using the SIMBAD Database and HASH PN database (Parker et al. 2016, hashpn.space) to identify known SNRs, PNe and H II regions (Filipovic et al. 1998a). The SNRs and PNe found here are addressed in Filipović et al. (2009) and Bozzetto et al. (2017) and are excluded together with all known H II regions from the catalogue presented in this paper.

(iv) The ATCA 1.384 GHz source list was taken as the starting point which for the cross-match with the other source lists extracted from the above listed radio surveys. We use a nearest neighbour matching radius of 30 arcsec to determine whether there was a detection at any other frequencies. With a secondary internal match we were able to identify sources that have multiple components at the higher frequencies of 4.8 and 8.64 GHz, while being unresolved at the lower frequencies, 0.843 and 1.384 GHz. After each cross-match, a best match position was created for each source to aid in subsequent cross-matching. This best-match position is taken from the highest-resolution component for the source.

(v) A second and final, targeted source finding sweep was conducted on all images using prior knowledge from three ATCA source lists. We also apply this prior knowledge where the source does not have a detection above 5σ for the image in question. Consequently, this allows for a second source finding pass to detect sources down to 3σ and cross-matching (and merging) these into the existing source lists.

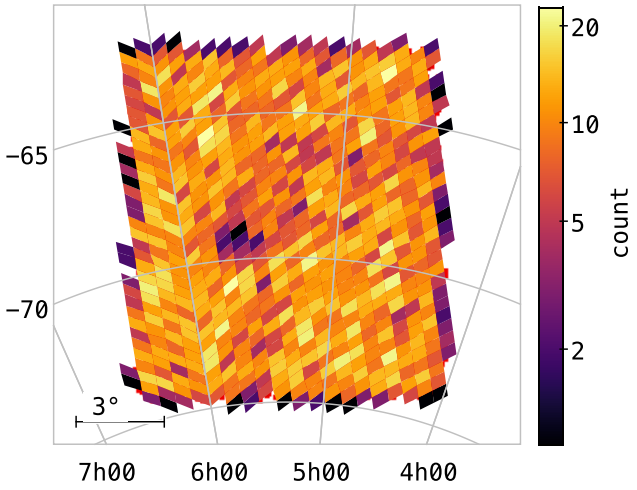

Figure 1. A map of the source counts in HEALPix pixel map in equatorial coordinate system (X axis is RA J2000 and Y axis is Dec J2000). The map is produced using TOPCAT with HEALPix level 7 (pixel area is ≈ 0.21 deg^2). As scale bar shows, black coloured pixel indicate low density source population which is in agreement with intentionally avoided fields such as the 30 Dor and outer edge of the survey where our coverage is limited.

We estimate a false cross-match rate of ∼1 per cent by shifting each source list in RA by three times the cross-matching criterion. For example, the 4.8 GHz to 1.384 GHz cross-match radius is 30 arcsec, hence we shift the 4.8 GHz image northward by 90 arcsec

and repeat the cross-matching procedure. This removes any real matches so that we are left with only random matches.

Supplementary source lists have been added to more accurately constrain the spectral index of each source as described in Sect. 2.6. AT20G was the first of these supplementary source lists to be cross-matched with all of the preceding surveys. The addition of this source list reveals a limited number of sources (38) but provides a significant increase in the positional accuracy and a wider frequency range which is essential to a better constrained source spectral energy distribution (SED). The best-match position was then replaced with the position from the highest angular resolution survey. In line with this, the next supplementary source list to be added was the SUMSS catalogue, as it had the next best resolution. Similarly, the best match position was recalculated before repeating this cycle with the MWA, MRC and PMN source lists. The PMN catalogue was cross-matched with a 252 arcsec search radius due to its poor resolution compared to our other surveys. Unlike for the four core radio surveys (SUMSS at 0.843 GHz and ATCA at 1.384, 4.8 and 8.64 GHz), a further internal cross-match was not performed on these supplementary surveys.

Multiple cross-matches of a source may be present throughout each of the source lists that have been acquired from existing surveys or generated through Aegean. This is due to the differing resolutions of each image, allowing for one detection to be resolved into multiple detections at higher frequencies. These sources have been flagged in our source lists and catalogued as "Confused Source". Sources of this nature have been excluded from the following analysis, because of their complexity.

Care must be taken when cross-matching these detections due to the differing resolutions and positional accuracies, both of which create false matches. These false matches and erroneous data points can be potentially corrected by understanding trends in the cross-match between different pairs of catalogues as shown in Sections 3.2, 3.3 and 4.3.1. Once identified, a manual approach (source-by-source visual inspection) is used to investigate the erroneous properties bf such as flux density, spectral index and exact position. This cycle of analysis is vital in creating a reliable catalogue.

Additionally, extensive cross checking with the Magellanic Cloud Emission Line Survey (MCELS) in Hα, [SII], and [OIII] images presented by Smith & MCELS Team (1998) has been performed to identify sources in both the optical and radio bands. These matches are most likely intrinsic to the LMC (see for example Yew et al. 2021). Radio sources with optical counterparts as detected in MCELS have been excluded from further analysis in this work. We note that the MCELS images have been continuum subtracted and no compact stellar optical sources can be detected. Hence, these objects detected in the MCELS images are likely to have an LMC origin and will be studied in our subsequent papers. Also, we make use of other existing optical catalogues that have known background sources, as determined from their redshifts (discussed in Sect. 4). 98 such radio sources from the MCELS have extended emission (optically diffuse objects) while 129 sources have a compact optical object at or near the centre of the radio source. An additional cross check was made with known objects, such as 80+ SNRs, 20+ PNe and 100+ H II regions. Variable sources may be present but are hard to detect as this catalogue has been compiled from datasets with sparse coverage over a long time-scale (~31 years).

A sample of the final catalogue is shown in Table 3. This table includes our combined selected radio source lists from all surveys apart from two 0.843 GHz lists from ASKAP-Beta and MOST surveys as discussed in Sects. 3.4.2 and 3.4.3. The first column of Table 3 is using the standard International Astronomical Union (IAU) source naming format of Jhhmmss–ddmmss (Dickel 2000). This name has been derived from the position of the highest resolution detection for each source from all input source lists. Columns 2 and 3 give the source position from the highest-resolution detection of the source. The full catalogue is available through the VizieR Catalogue Service (Ochsenbein et al. 2000). For each survey in the final combined catalogue, we provide a source position, size, integrated flux density, peak flux density and a local rms measure. From this, we calculated a spectral index (α) where possible which is defined as $S_\nu \propto \nu^\alpha$, where S_ν is flux density at frequency ν.

3.2 Selection Effects and Completeness

Our catalogue of discrete radio sources presented here is not complete because of various problems including (but not limited to) detection limits, diffuse emission from the LMC, imaging artifacts, variable and changing sensitivity (across the field of a given survey) as well as the resolution limitations for both foreground and background objects. This is most notable in the 30 Dor region where large side-lobes are produced by strong and diffuse emission, especially in our ATCA images. This area has been excluded from the analysis to prevent contamination from this emission and the spurious clean components created during the imaging phase (see Figure 1). We define this exclusion area around 30 Dor after inspecting the 1.384 GHz and 0.843 GHz images and then we applied this exclusion to all subsequent source finding catalogues. This is the area between RA(J2000) of $5^h30'$and 5^h47^m and Dec(J2000) from $-68°50^m$ to $-70°$. The rms estimates presented in this work are the best case measurement, i.e. taken from source free regions on the outskirts of the LMC. As mentioned above (Sect. 3.1), we have excluded all known SNRs and H II regions listed by Bozzetto et al. (2017) and various other surveys covering sources that are a part of the LMC. This has allowed us to have a less contaminated population of background (such as Quasars and AGN) and foreground objects (mainly Galactic radio stars).

3.3 Discrete Source Finding Errors

It is widely accepted that all source finders have an error rate[2] of at least a few per cent. However, this depends a lot on the threshold settings. The compromise is always between completeness (of real sources) and reliability. Aegean is no exception to this, as shown in Hopkins et al. (2015). The catalogue from each image was carefully visually inspected for spurious sources due to image artifacts and regions of strong emission. For example, detections were made along the edge of each image which were either incomplete or false detections, requiring a manual pass to remove these sources. This manual pass was extended to the catalogue as a whole, with a focus on regions of strong emission (either sidelobes or extended emission) and sources with unrealistic properties (such as extremely large gaussians, strong sources and source positions beyond the limits of the observed area).

3.4 Discrete Source Position and Integrated Flux Density Uncertainties

The richness of data available for this field allows us to compare and, if necessary, post-calibrate our new source lists. This was par-

[2] Includes the number of false positives and the missing real sources.

ticularly useful for the ASKAP-Beta data, which was re-calibrated against the more reliable SUMSS catalogue.

3.4.1 *ASKAP-Beta and MOST Survey Positional Correction*

To determine the positional accuracy of the ASKAP-Beta data set, we have made comparisons with the SUMSS 0.843 GHz source list. From this, we find that the ASKAP-Beta dataset requires a ~3 arcsec correction of its source position to be consistent with existing catalogues. Larger offsets are found when comparing the ATCA 1.384 GHz catalogue with the ASKAP-Beta catalogue as the median positional offset between the two catalogues is 4.23 and 0.36 arcsec in RA and Dec respectively. A similar discrepancy is identified when positional comparisons are made with the 0.843 GHz MOST source list. The median positional offsets are 2.79 and 0.72 arcsec in RA and Dec, respectively, as shown in Figure 2. The cross-matching process was performed after correcting the positional error. A comparison of positional offsets between pairs of catalogues is shown in Figure 2.

3.4.2 *ASKAP-Beta Flux Density Post-Calibration*

We make use of the SUMSS survey as an established, external catalogue in order to determine the completeness and quality of our newly produced source lists of ASKAP-Beta and MOST surveys.

It is now understood that the ASKAP-Beta system and, by extension, the observations made during that time had an inaccurate amplitude calibration on the order of ~10 – 15 per cent. This affected the flux density measurement and caused an additional positional offset (Sect. 3.4.1).

A systematic correction was derived from the comparison with the SUMSS survey as no frequency interpolation is required to compare fluxes. Additionally, we have used the SUMSS catalogue to measure the completeness and reliability of the 0.843 GHz MOST source list (as shown in Sect. 3.2). Using these surveys, we perform a least squares linear fit to determine the systematic positional offset present within the ASKAP-Beta dataset. Before correcting these data, the ratio of $S_{\rm ASKAP-Beta}/S_{\rm MOST}$ for the integrated flux was 0.880; similarly the ratio of $S_{\rm ASKAP-Beta}/S_{\rm SUMSS}$ was 0.893. From these results, we have applied a 12.75 per cent systematic increase to the ASKAP-Beta fluxes.

Even after applying the above corrections however, at lower flux densities ($< 15\sigma$) our ASKAP-Beta flux densities still show a large variance. In Figure 3a we show a direct comparison between the estimated flux densities and histograms of the flux density differences normalised to the weighted root sum square of the corresponding uncertainties (see section 4 of Gregory & Condon (1991)). The plots clearly show that the deviation from the expected value is significant and it appears to be a non-linear systematic function of the flux density (i.e. the lower ASKAP fluxes appear to be systematically underestimated). Not just flux scale, but poorly known ASKAP beam shapes are a huge problem. The primary beam correction factors were poorly known and variable at the time of testing.

The resulting source list is provided in Table 4. While we found that this list is useful for the confirmation (and detection) of faint sources, we decided not to use the ASKAP data in the following analysis and in our combined catalogue shown in Table 3. we also note the problem that S_{int}/S_{peak} is systematically higher than one, by typically 20 per cent.

3.4.3 *MOST Survey Flux Density Post-Calibration*

The SUMSS survey reaches a rms of ~1 mJy beam^{-1} allowing for ~78 per cent (1638 sources) of sources in the 0.843 GHz MOST source list to be cross-matched and compared against the sources within SUMSS. From this, we find that all SUMSS sources have an 0.843 GHz MOST counterpart (within the overlap region). However, not all 0.843 GHz MOST sources within the same limits (rms and spatial) have a SUMSS detection. As expected, we detect an additional 446 sources in the 0.843 GHz MOST image that are undetected in SUMSS.

These 1638 sources common to both lists, allow us to determine the flux density accuracy of our 0.843 GHz MOST sources (as shown in Figure 3b). The ratio of the integrated flux densities for these two surveys ($S_{\rm SUMMS}/S_{\rm MOST}$) is 1.02±0.01. This ratio does not show any systematic offset between two source lists. In Figure 3b (lower right panel) we can see that the distribution of normalised flux density differences are much wider than acceptable.

As for the ASKAP-Beta flux density analysis, we can use the MOST detections for cross-checking of faint source detections. However, we are not using these flux densities in source spectral index estimates and in constructing our main catalogue Table 3. We present the MOST 0.843 GHz source list with its positions and all measured flux densities as a separate Table 5.

3.4.4 *Other Flux Density Errors and Uncertainties*

Uncertainties in flux density estimates are mainly a product of gain calibration uncertainties (σ_g; usually given as a percentage of the measured flux density S) and the uncertainty (σ_n) caused by fitting in the presence of the local noise. The total uncertainty (σ_{tot}) can be then calculated as:

$$\sigma_{tot}^2 = \sigma_n^2 + (S \cdot \sigma_g)^2 \quad (1)$$

We applied a 10 per cent uncertainty in the gain (σ_g) to our new ATCA flux estimates at 1.384, 4.8 and 8.64 GHz, as recommended in Harvey-Smith et al. (2018).

All source finding tools have a degree of error in their flux density estimation (see also Sect. 3.3). The main source of this inaccuracy is due to the noise present within any image, causing the sources at or near the detection threshold to have large flux density errors as shown in Figure 4. In addition to this effect, source finding tools can incorrectly determine the extent of a source, and in most cases will overestimate source flux density (Hopkins et al. 2015).

To determine this, we measure the error of the integrated flux density as a function of fitting error (σ_n) to find outlier sources that have been fitted poorly, as shown in Figure 4. As expected, the relative error increases with weaker sources. Statistically, σ_n for the majority of our sources is less than 15 per cent across all five main catalogues. However, for some smaller portion of sources it can reach up to 30 per cent.

3.4.5 *MWA Survey Flux Density Post-Calibration*

The radio images presented by For et al. (2018) were processed by Hurley-Walker et al. (2017) as part of a large analysis of the GLEAM survey to produce an extragalactic catalogue. During the flux density calibration of the final mosaics of the GLEAM survey, a correction was made for the primary beam of the instrument, which was poorly modelled at the time of processing. This was performed by measuring the ratio of flux density of sources between GLEAM

Table 3. Excerpt of the point source catalogue of 6 434 objects in the directions of the LMC with its positions, integrated flux densities with associated uncertainty and spectral index. The columns provided are as follows: (1) Source name derived from the highest frequency source component; (2) position of J2000 right ascension from the highest frequency detection; (3) position of J2000 declination from the highest frequency detection; (4) flux density flag for the GLEAM survey; (5 & 6) GLEAM MWA 200 MHz survey integrated flux density; (7 & 8) SUMSS 843 MHz survey integrated flux density; (9) flux density flag for the 20 cm ATCA 1.384 GHz survey; (10 &11) 20 cm ATCA 1.384 GHz survey integrated flux density; (12 & 13) 6 cm ATCA 4.85 GHz survey integrated flux density; (14 & 15) 3 cm ATCA 8.64 GHz survey integrated flux density; (16 & 17) MRC 408 MHz survey integrated flux density; (18 & 19) PMN 4.8 GHz survey integrated flux density; (20 & 21) AT20G survey integrated flux density at (20 & 21) 4.8 GHz; (22 & 23) 8.6 GHz; (24 & 25) 19.904 GHz; (26 & 27) spectral index fit to all available source components with the associated error; (28) number of flux densities used in the spectral index fit and (29) source classification. Upper limits and uncertain values in flux densities flag columns are designated with preceding < and colon (:), respectively. The columns not presented in this table but available in the full version are: flux densities from MRC, PMN and AT20G surveys. The full catalogue is provided through the VizieR service.

(1) Name J	(2) RA (J2000)	(3) DEC (J2000)	(4, 5 & 6) $S_{\rm MWA}$ 0.200 GHz (mJy)	(7 & 8) $S_{\rm SUMSS}$ 0.843 GHz (mJy)	(9, 10 & 11) $S_{\rm 20cmATCA}$ 1.384 GHz (mJy)	(12 & 13) $S_{\rm 6cmATCA}$ 4.85 GHz (mJy)	(14 & 15) $S_{\rm 3cmATCA}$ 8.64 GHz (mJy)	(...)	(26 & 27) $\alpha \pm \Delta\alpha$	(29) Class
...	...	...	...	...	...	...	...	...	...	
053145–721857	05:31:45.9	–72:18:57	165 ± 17	41.2 ± 1.6	24.9 ± 2.5	...	...	...	–0.98 ± 0.07	...
051637–723707	05:16:37.8	–72:37:08	319 ± 16	261 ± 11	230 ± 23	...	...	...	–0.03 ± 0.02	HFP
054427–715526	05:44:27.2	–71:55:27	982 ± 18	334 ± 10	213 ± 21	55.1 ± 5.5	21.7 ± 2.2	...	–0.99 ± 0.02	...
060531–711229	06:05:31.3	–71:12:29	230 ± 19	93.9 ± 3.1	75.9 ± 7.6	...	...	...	–0.32 ± 0.02	...
055632–712906	05:56:32.2	–71:29:06	558 ± 21	189.7 ± 5.8	115 ± 12	33.0 ± 3.3	14.9 ± 1.7	...	–0.93 ± 0.03	...
...	...	...	...	...	...	...	...	...	...	
054749–635200	05:47:49.1	–63:52:01	80 ± 22	19.5 ± 1.3	9.4 ± 1.0	...	...	...	–1.08 ± 0.16	...
054831–654816	05:48:31.0	–65:48:17	146 ± 25	39.0 ± 1.4	22.2 ± 2.2	6.6 ± 1.1	...	...	–0.98 ± 0.07	...
054845–655349	05:48:45.1	–65:53:50	584 ± 78	116.6 ± 3.6	70.9 ± 7.1	17.2 ± 1.8	7.6 ± 1.0	...	–1.14 ± 0.04	...
054845–665725	05:48:45.6	–66:57:25	173 ± 28	60.0 ± 1.9	38.7 ± 3.9	16.2 ± 1.7	7.1 ± 1.1	...	–0.82 ± 0.05	...
054850–625443	05:48:50.2	–62:54:43	<51	18.6 ± 1.2	:10.5 ± 1.2	...	...	...	–1.13 ± 0.23	...
054919–643738	05:49:19.5	–64:37:38	110 ± 21	32.9 ± 1.3	19.1 ± 1.9	...	...	...	–0.89 ± 0.11	...
...	...	...	...	...	...	...	...	...	...	

Table 4. Excerpt for the source list (total of 1 995 sources) at 0.843 GHz derived from ASKAP-Beta survey. Note that the flux densities shown are flux corrected (see text for more details). The uncertainties are only from the fitting method i.e. flux calibration errors have not been included in the presented uncertainty.

No	RA (J2000)	DEC (J2000)	Peak (mJy beam^{-1})	Int. Flux (mJy)	Local rms (mJy beam^{-1})
1431	05:58:22.4	–65:07:23	34.7 ± 0.8	40.2 ± 0.9	0.78
1432	05:58:23.2	–67:55:28	9.1 ± 0.6	9.6 ± 0.7	0.65
1433	05:58:23.9	–67:18:23	5.2 ± 0.6	7.0 ± 0.8	0.59
1434	05:58:25.3	–66:05:16	22.2 ± 0.7	27.5 ± 0.8	0.69
1435	05:58:28.4	–68:24:37	22.5 ± 0.7	30.0 ± 1.0	0.76

Table 5. Excerpt for the source list (total of 2 084 sources) at 0.843 GHz derived from MOST. The uncertainties are only from the fitting method i.e. flux calibration errors have not been included in the presented uncertainty.

No	RA (J2000)	DEC (J2000)	Peak (mJy beam^{-1})	Int. Flux (mJy)	Local rms (mJy beam^{-1})
1116	05:24:32.4	–66:42:36	26.0	29.5 ± 0.3	0.7
1117	05:24:41.8	–71:01:33	14.0	14.0 ± 1	0.75
1118	05:24:41.7	–67:18:07	19.0 ± 2	19.2 ± 0.2	1.17
1119	05:24:46.7	–70:25:19	4.0	4.0	0.59
1120	05:24:48.5	–65:15:57	13.0 ± 1	13.2 ± 0.1	0.61

and ancillary catalogues in the Northern sky, then assuming symmetry and applying this correction to the Southern sky. At declinations far from the local zenith ($\delta \sim -27^\circ$) the correction was less accurate, resulting in an estimated flux density calibration accuracy of 8 per cent for $-72^\circ < \delta < 18^\circ$ and 13 per cent outside of this range, escalating to $\approx$ 90 per cent at the celestial pole.

The GLEAM data comprise a "wideband" 170–231 MHz image, typically used for source detection, and 20×7.68 MHz "sub-band" images, covering 72–231 MHz. In the catalogue formed by Hurley-Walker et al. (2017), sources detected in the wideband image at peak flux density $> 5\sigma$, where σ is the local rms noise, are measured in the sub-band images using the *priorised* fit function of AEGEAN (Hancock et al. 2018). We used an identical procedure to Hurley-Walker et al. (2017) to produce a catalogue for this region of sky, including accurate rms, background, and PSF measurement. Note that from these multi-frequency data, SEDs can be measured for brighter sources, enabling a more accurate flux density measurement, but for fainter sources the spectra are biased towards being flat by the uncertainties, and the wideband images provide the best measurement of the integrated source flux densities, which we here label as $S_{\rm 200MHz,GLEAM}$.

The high-frequency data presented in this paper enable us to test the flux density scale accuracy and recalibrate the GLEAM data. We first selected sources which would not be confused in the MWA

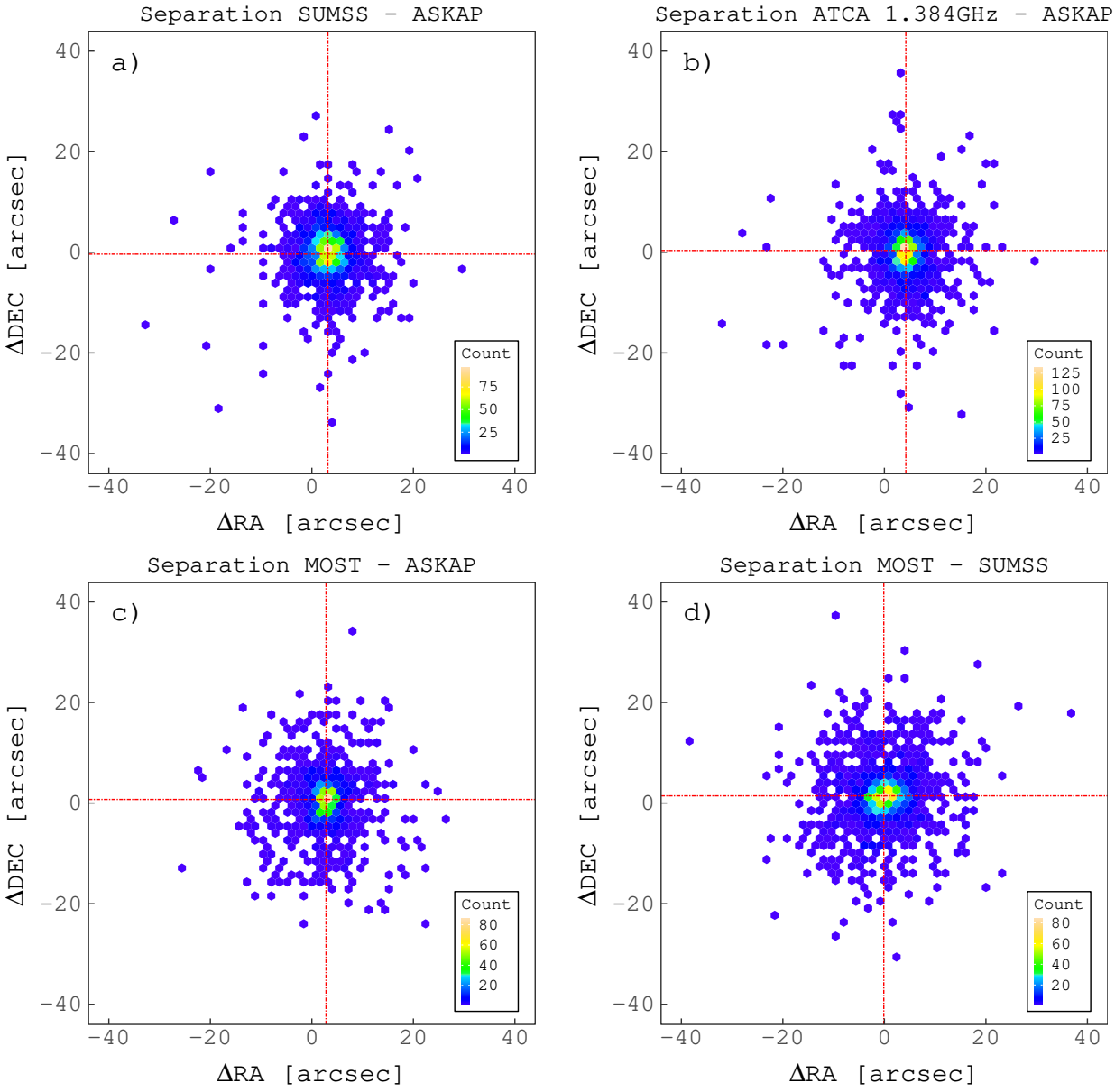

Figure 2. Positional comparisons between **a)** SUMSS – ASKAP-Beta, **b)** ATCA 1.384 GHz – ASKAP-Beta, **c)** MOST – ASKAP-Beta and **d)** MOST – SUMSS catalogues without applying ASKAP-Beta positional corrections. The median RA and Dec offsets are shown with vertical and horizontal red dot-dashed line, respectively. The median positional offsets in RA and Dec, respectively, are: **a)** 3.18 and -0.36 arcsec, **b)** 4.23 and 0.36 arcsec, **c)** 3.18 and -0.36 arcsec and **d)** -0.11 and 1.44 arcsec.

data by excluding any sources within 2 arcmin of any other source, yielding a catalogue of 5 419 sources. For each source we fitted a weighted linear power-law SED using the *scipy.stats.leastsq* implementation of the Levenberg-Marquardt algorithm to all of the high-frequency data. From these fitted spectra we predicted the 200-MHz integrated flux densities, $S_{200\mathrm{MHz,predicted}}$. We crossmatched these sources with the results from the GLEAM source-finding, yielding 1 178 matches within 2 arcmin positional threshold. From these we excluded the sources with GLEAM $S_{200\mathrm{MHz,GLEAM}} > 1$ Jy, leaving 43 sources with high signal-to-noise and clean SEDs. We compared the predicted flux densities to those measured by GLEAM in the wideband image, finding that $S_{200\mathrm{MHz,GLEAM}} = (0.80 \pm 0.13)\ S_{200\mathrm{MHz,predicted}}$. We applied this factor to the final cross-matched ensemble of GLEAM integrated flux densities, yielding the 200-MHz measurements referred to as "GLEAM" in Table 1.

We used the Positional Update and Matching Algorithm (PUMA; https://github.com/JLBLine/PUMA; Line et al. 2017)) to establish the final cross-match between GLEAM and our main catalogue. PUMA is an open source software capable of cross-matching between radio surveys with different spectral (frequency) and resolving capabilities. The GLEAM catalogue was used as the base catalogue to match sources from our ATCA 1.384 GHz catalogue within 2 arcmin and in combination with objects catalogued in the SUMSS 843 MHz survey. Since PUMA relies on spectral characteristics of cross-matched sources, as well as on their positions, we used the newly re-calibrated GLEAM flux densities as described above. We adopted as positive matches all sources flagged by the PUMA algo-

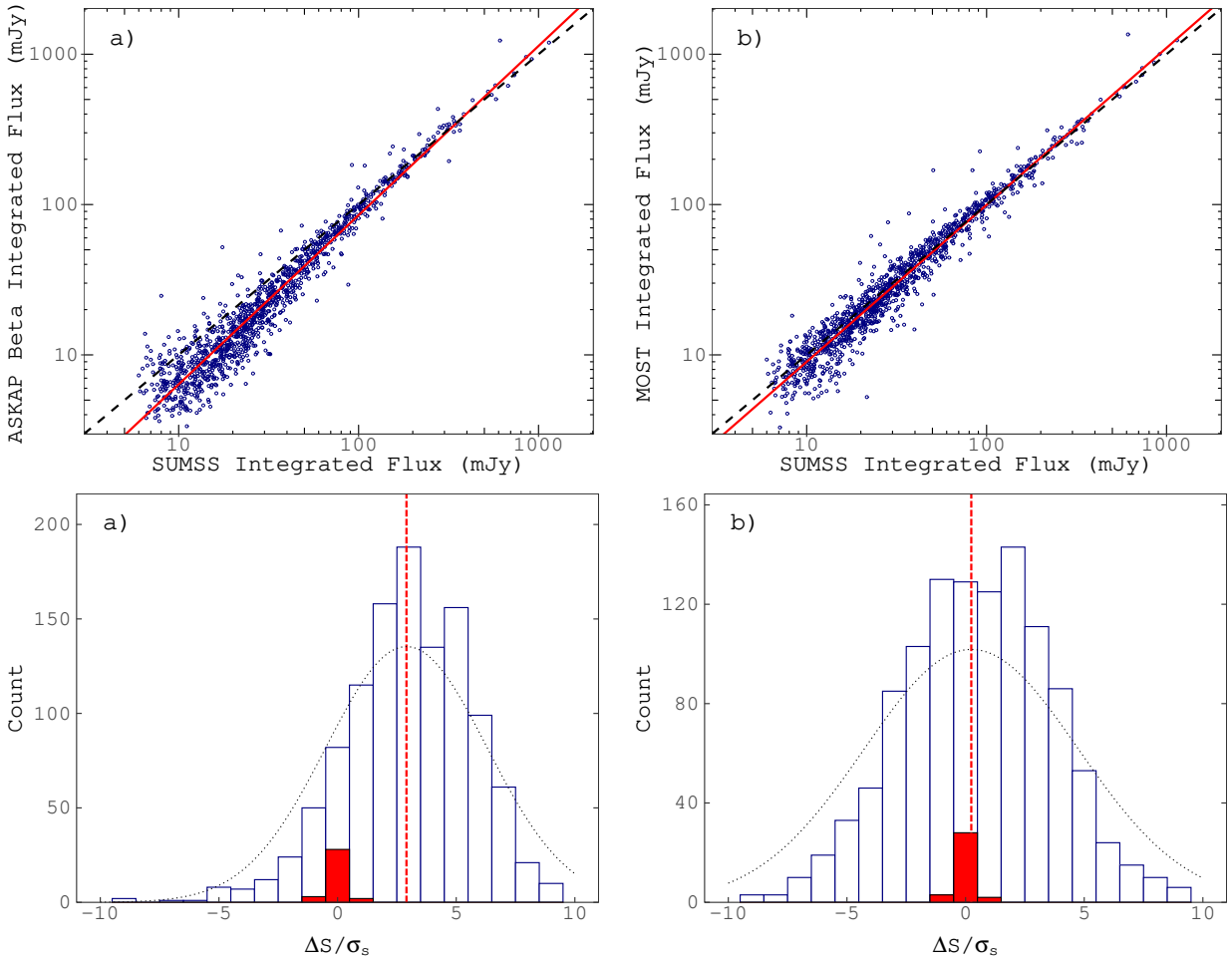

Figure 3. Top row: An integrated flux density comparison of the ASKAP-Beta (a) and MOST (b) 0.843 GHz source lists, with the SUMSS (see Sects. 3.4.2 and 3.4.3 for more details). In each figure, we represent a ratio of 1 with the black dashed line and the best fit line is in red. **Bottom row:** Histogram of flux density differences weighted with the root sum of squares of corresponding uncertainties. Histogram has a bin size of 1 normalised flux difference. Vertical red dashed line represents the mean of the distribution. Dotted line is a Gaussian distribution with the same mean and standard deviation as in the histogram. Red-filled histogram show the distribution of $\Delta S/\sigma_s$ between matched sources from PMN and ATCA (Dickel et al. 2005), respectively, at 4.8 GHz.

rithm as (a) isolated, i.e. only single cross-match is found within the search region, or (b) dominant, i.e. multiple cross-matches are found but one matched source fits a power law significantly better than the others (see the PUMA manual[3] for more details). We found a set of 255 sources flagged as *multiple*, consisting of multiple higher resolution (see Sect. 3.5) sources blended into a single GLEAM source. For these objects we have used GLEAM flux densities as upper limits for cross-matched, high resolution, components.

Finally, sources fainter than the source detection limit of 5σ are considered undetected, and their flux density in our catalogue is given as an upper limit as 5σ, with the rescaling factor applied. We provide an additional column in the electronic catalogue with flag (<) designating an upper limit for the flux density.

3.5 Spectral Index Uncertainties

Spectral index (α) is defined in Sect. 3.1. We use R's package METAFOR (Viechtbauer 2010) to estimate α using an unweighted mixed-effects linear regression model. The model takes into account uncertainties in the flux measurements to estimate α uncertainties. If no uncertainty is reported in the original measurement we assumed 10 per cent of the flux value. Large uncertainties in spectral index ($\Delta\alpha > 0.5$) are mainly the result of only two frequencies available.

[3] https://github.com/JLBLine/PUMA

4 RESULTS AND DISCUSSION

4.1 Optical and Radio Counterparts

We make use of multiple optical catalogues (as described in Table 2) and we find 7 883 unique optical sources that are thought to be sources behind the LMC. We apply a 5 arcsec search radius when matching optical counterparts to the highest frequency radio component. From this, we find 343 unique optical sources (Table 6) of which 128 have a spectroscopic redshifts. For these 128 sources, we calculate a mean redshift of 0.39. The average positional offset between the radio continuum and optical sources is 1.59 and 1.72 arcsec in RA and Dec respectively.

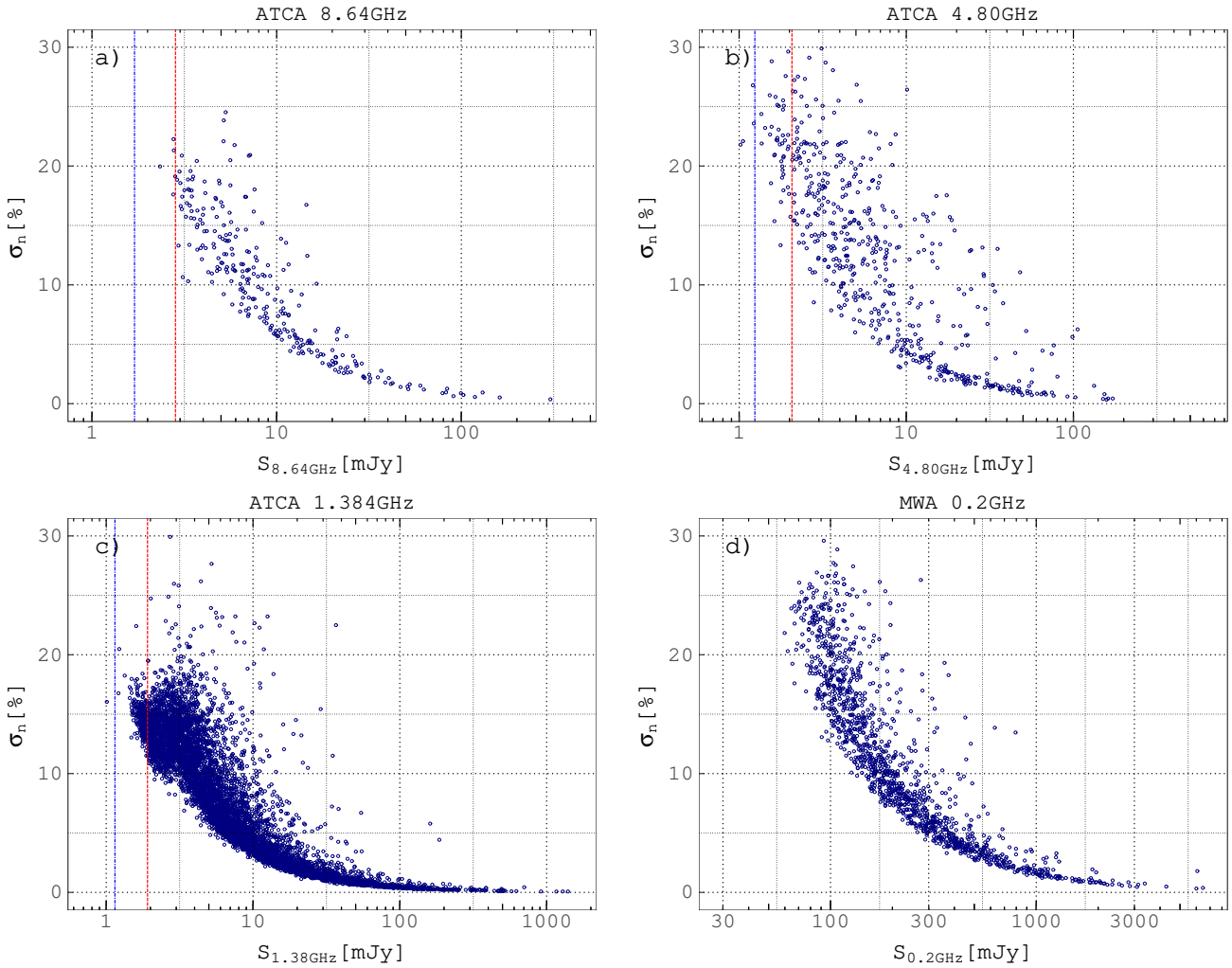

Figure 4. The fitting flux density error (σ_n) for each source as a per cent of the total integrated flux density. The blue dot-dashed line represents the 3σ rms limit of each catalogue, and the 5σ cutoff is shown with a red dotted line.

Table 6. Excerpt of the list (total of 343 sources) of sources from our base catalogue cross-matched with six optical surveys used in this study (see Sect. 2.6). We provide the name of the source as defined in Table 3, catalogued redshift value and the associated reference (columns z and z Ref. and the references to optical detection (Det. Ref.)). Number-coded references are: (1) 6dF: Jones et al. (2009), (2) MACHO: Kim et al. (2012), MQS I: Kozłowski & Kochanek (2009), (4) MQS II: Kozłowski et al. (2012), (5) MQS III: Kozłowski et al. (2013) and (6) MCELS: Smith & MCELS Team (1998).

Name J	z	z Ref.	Det. ref.
...	...	...	...
043259-713059	0.04383	1	1
043359-695840	0.06808	1	1
043429-694910	...	...	3
043436-693615	...	...	6
043436-705252	...	...	6
043442-691448	...	...	6
043521-722117	...	...	6
043523-690349	0.061	5	3;5
043555-722838	0.04391	1	1
043642-664254	0.02948	1	1
...	...	...	...

4.2 AGN Populations

Kauffmann et al. (2003) used the Sloan Digital Sky Survey to argue that AGN of all types and luminosities are typically found in the most massive galaxies. They also concluded that the optically luminous AGN reside in galaxies with younger stellar populations with strong indications of recent starburst activity.

A subset of this population are the radio-loud AGN which form highly collimated, fast jets of material that drive through the surrounding galaxy into the intergalactic medium, at close to the speed of light. This class of AGN can be further divided into Quasars, BL Lacertae Objects (BL Lac) or Flat Spectrum Radio Quasars (FSRQ), Optically Violent Variable Quasars (OVV) and Radio Galaxies. Even though these jets are seen to primarily emit synchrotron radiation, their composition and production mechanism are still widely debated. These different classifications are thought to describe similar host galaxies (AGN) seen at different orientation angles with respect to our line of sight, creating differences both in the observed radio morphology as well as the optical activity type (Antonucci 1993; Urry & Padovani 1995; Urry 2003; Kazanas et al. 2012).

We use the definition from Sadler et al. (2006) to categorise the emission mechanisms of a source by its spectral index for centime-

tre wavelengths, i.e.: flat-spectrum sources with an $\alpha > -0.5$ are thought to be dominated by self absorbed, compact objects, while sources with $\alpha < -0.5$ are dominated by optically thin synchrotron emission (Collier et al. 2018; Galvin et al. 2018).

4.2.1 GPS and CSS Sources

GPS and CSS sources are thought to contribute ~30–40 per cent of radio sources (An & Baan 2012; Lonsdale et al. 2016). However, their true nature is still under discussion. The debate about the absorption mechanism that contributes to the unique spectral features of this population has continued for over thirty years. The most extensive study of GPS and CSS sources is presented by O'Dea (1998) and more recently O'Dea & Saikia (2021) who hypothesised regarding their origin. They additionally use these sources as constraints on AGN physical evolution as it is believed that these sources represent the early stage of the AGN phase (Fanti et al. 1995; Polatidis & Conway 2003; Fanti 2009; Randall et al. 2011; Callingham et al. 2017; Collier et al. 2018).

GPS and CSS sources are usually small (point) radio sources without jets and have similar characteristics in that they are both compact with steep spectra ($\alpha < -0.8$). GPS sources have a much higher turnover frequency apart from their steep spectrum beyond the turnover frequency. This observable property allows their physical size to be estimated using the relation shown by Orienti & Dallacasa (2014) who agree with previous work by O'Dea & Baum (1997, Eq. 4). They define the relation (fit) as:

$$\log \nu_m = (-0.21 \pm 0.05) - (0.65 \pm 0.05) \log \mathrm{LLS} \quad (2)$$

where ν_m is the turnover frequency (in GHz) and LLS is the largest linear size (in kpc). This suggests a simple physical process common to both GPS and CSS populations that have been separately defined due to an arbitrary selection of turnover frequencies. Generally, it is believed that these objects are young, whose growth was frustrated by dense gas and dust or are simply young radio sources moving along their evolutionary path. Fanti et al. (1995) presented the "young source" hypothesis, postulating that these sources typically have ages of 10^6 years and tend to decrease their radio luminosity with time and grow in size from a few kpc to a few hundred kpc.

CSS sources are classified as such if they show an α of < -0.8, while GPS sources have an average α of +0.56 below the turnover frequency and −0.77 above the turnover. In this study we detected 1 866 CSS candidate sources with an α of < -0.8, indicating candidates for further analysis as discussed in Sect. 4.3.

4.2.2 High Frequency Peakers (HFP)

We follow the convention given by Dallacasa et al. (2000) in naming radio continuum sources with spectra that peak above 5 GHz, HFPs. These high-frequency peaking sources are thought to be very young and compact, following the anti-correlation shown in Equation 2. Additionally, these sources are thought to be rapidly changing in radio flux density, size and flux density peak frequency on time scales of a few decades. These sources are thought to then evolve into GPS sources, then become CSS sources and finally evolve into Large Scale Objects (LSOs) with a significantly broader (flatter; less peaked) spectrum (Fanti et al. 1995; Readhead et al. 1996; Alexander 2000; Marecki et al. 2003; Orienti & Dallacasa 2008; An & Baan 2012).

Dallacasa et al. (2000) presented a catalogue of 55 HFP sources above 300 mJy near the peak frequency of 4.9 GHz, with the majority of these being unresolved sources at small angular scales. Additionally, they defined a sample of true HFPs as sources with an $\alpha < -0.56$ above the turnover frequency. Understanding and modelling these sources is of vital importance for three main reasons: **1)** their evolutionary path is currently not very well understood; **2)** these sources are highly variable on short time scales, with this change likely driven by significant events in their host galaxy; **3)** due to the high frequency of their emission peak, these sources can strongly contribute to measurements of the Cosmic Microwave Background (CMB) radiation as observed with the WMAP and PLANCK telescopes and as such these sources need to be accurately subtracted (De Zotti et al. 2000). Dallacasa & Orienti (2016) show that a common behaviour of HFP sources is a spectral profile change (a change in time of the shape of the radio spectrum) correlated with an increase in optically thick emission and a decrease in optically thin emission.

We find 14 potential HFP characterised by an inverted spectrum (i.e. $\alpha > 0.5$) and a possible turnover in their radio spectrum above 5 GHz, as discussed in Section 4.3.3.

4.2.3 FSRQ and BL Lac Candidates

We investigated the sample of blazar candidates behind the LMC as presented by Żywucka et al. (2018). They identified 37 such objects (their Tables 2 and 3) of which 23 are classified as FSRQ candidates and 14 are BL Lac candidates. Using a 30 arcsec search radius, we find 17 out of 23 FSRQ have a radio counterpart in common with the catalogue presented here (Table 3), and 9 out of 14 BL Lac candidates in common. We note that all 11 objects (6 FSRQ and 5 BL Lac candidates) that are not detected in our surveys are listed in Żywucka et al. (2018) as "dubious objects".

We denote these sources in our radio catalogue as the FSRQ or BL Lac accordingly (Table 3; Col. 13). The FSRQ candidate sample has a mean α of –0.43 ±0.12 (compared to Żywucka et al. (2018) findings of –0.40 ±0.09) while the BL Lac sample has a somewhat steeper mean α of –0.72 ±0.13, and a combined α of –0.53 ±0.20. This is expected to be flatter than the average AGN population ($\alpha = -0.89$; Table 8) as discussed in Sect. 4.3. We note that BL Lac objects are known to be highly variable and as such their spectral indices should be treated with caution as our radio continuum data were not obtained simultaneously. Additionally, we estimate the average optical redshift of FSRQ sample studied here is 1.37±0.17 based on various z measurements described in Sect. 2.6.

4.2.4 IFRSs and HzRG Candidates

Finding High Redshift Radio Galaxies (HzRGs) is important in understanding the formation and evolution of galaxies at higher redshifts and in dense environments. Traditionally, radio sources with an Ultra Steep Spectrum (USS) ($\alpha < -1.3$) have been the most efficient tracers of HzRGs at $z > 2$. This technique is based on the observed steepening of the radio spectrum with both redshift and frequency. Almost all known HzRGs including the most distant one at $z = 5.72$ (Saxena et al. 2018) have been identified using the USS selection method only. However, several studies Yamashita et al. (2020); Jarvis et al. (2009); Waddington et al. (1999) demonstrated that the USS selection criterion is not fully efficient as they discovered radio galaxies with flatter spectral indices. Finding high redshift radio-AGNs without relying on USS selection technique is now possible with the discovery of Infrared Faint Radio Sources (IFRSs) from the deep ATLAS radio continuum survey a decade ago.

IFRSs are a class of high redshift radio loud AGN originally identified as bright radio sources with no co-spatial IR counterpart when cross-matching the 1.4 GHz ATLAS radio survey with the deep SWIRE IR survey between 3.6 μm and 24 μm (Norris et al. 2006). As radio sources, the nature of IFRSs was unknown at the time. It was believed that all radio sources whether it is star forming galaxies or AGN would produce IR emission. Numerous follow up studies have been conducted since their discovery to select more IFRSs and to understand what they are. Since the original selection criterion from Norris et al. (2006) was survey specific, Zinn et al. (2011) redefined it and proposed a set of survey independent criteria, which even enable the selection of a brighter population of IFRSs with very faint IR counterpart. They have radio-to-IR flux density ratios above 500 and secondly, 3.6 μm flux density less than 30 μJy. To date, a total of ~1400 IFRSs have been identified from various radio surveys using the criteria of Zinn et al. (2011). All studies so far suggested that most of the known IFRSs, if not all, are radio-AGNs at $z > 2$. Orenstein et al. (2019) further confirmed the high redshift nature of IFRSs by presenting the largest sample of 108 IFRSs with median spectroscopic redshift of 2.68. Additionally, some studies presented the evidence that IFRS population not only encompasses USS sources but also flat spectrum sources too **(Collier et al. 2014)**. Thus, selecting IFRSs serves as a valuable technique to discover all sorts of high redshift radio-AGNs.

We search for high redshift radio AGNs behind the LMC by selecting the potential IFRS candidates following the procedures from Collier et al. (2014) and Orenstein et al. (2019) utilising the IR photometry from the CatWISE2020 (Marocco et al. 2021) and SAGE (Meixner et al. 2006) surveys. We cross-matched the radio sources in the LMC field with these two Mid-IR source catalogues, using a match radius of 1 arcsec. Because of the large radio beam sizes (~40 arcsec resolution), we chose 1 arcsec as the matching radius in order to minimise the false identifications. We acknowledge that by increasing the search radius we would certainly find many more true IFRS candidates but then the confidence level on these matches would be significantly lower.

A total of 123 IFRSs are identified in which 47 are found in SAGE, 71 in the CatWISE2020, and 5 in both. Out of 71 CatWISE2020 selected IFRSs 64 have a radio-to-IR flux density as defined by Zinn et al. (2011) larger than 500 at both 20 cm & 40 cm, 3 at 20 cm, and 11 at 40-cm only. Similarly, out of 47 SAGE-IFRSs 43 satisfied the Zinn ratio criteria at both 20 cm & 40 cm, and the remaining 4 at 40 cm only. The five IFRSs identified in both SAGE and CatWISE2020, all have ratios above 500 at both 20 cm & 40 cm. All of our IFRSs are found to have faint 3.4 or 3.6 μm counterparts which are reliably detected (S/N > 5) in either of the CatWISE2020 or SAGE surveys. In Table 7[4], we present our IFRSs sample. In Figure 5, we present the spectral index distribution of our IFRSs sample, which follows a skewed distribution towards steep spectral indices with a median of −0.96 – very similar to the distribution shown by Collier et al. (2014).

So far, only 131 IFRSs are known with spectroscopic redshifts lying in the range 1.63–4.4 (Orenstein et al. 2019; Collier et al. 2014). The only IFRSs in our sample with a measured redshift is J044537–685946 at $z = 1.714$ (Żywucka et al. 2018).

To date, only two IFRSs have been reported with an X-ray counterpart, suggesting that they are AGNs of Type I (Collier et al. 2014). We analysed whether any of our IFRSs from this study had been detected in the *XMM-Newton* survey (Haberl 2019), and three IFRSs were found to have an X-ray counterpart within 15 arcsec radius. They are J051233–675037, J050634–675643, and J052350–704213, which we plan to follow up for further studies.

[4] The full table will be in the supplementary material of the journal.

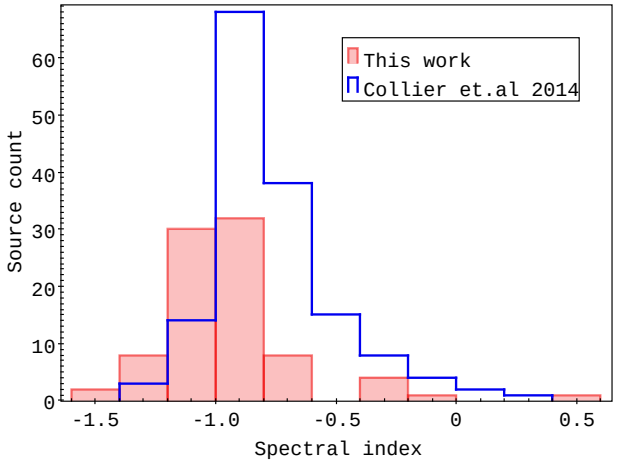

Figure 5. Radio spectral index distribution of our IFRSs sample in the field of the LMC, plotted as red solid boxes and IFRSs from Collier et al. (2014), plotted as blue dashed lines. Only sources with $\alpha_N \geq 3$ are plotted where α_N is the number of data points used to measure spectral index. Spectral index measurements in Collier et al. (2014) are based on 92, 20 and 6 cm data

Table 7. Excerpts of the table that list properties of 123 IFRSs studied here. Column 2 is source IR name or IDs from SAGE and/or CatWISE2020 catalogue; Column 5 represent 3.4–3.6 μm flux density. SAGE is 3.6 μm and CatWISE2020 3.4 μm

ATCA Name J	IR Source ID CWISE	$S_{1.4\,GHz}$ (mJy)	$S_{843\,MHz}$ (mJy)	$S_{3.6\,\mu m}$ (μJy)	α
054349-652228	J054349.72-652228.2	51.6	94.7	3.2	-1.0
055750-630159	J055750.40-630158.9	44.9	65.1	3.9	-0.63
051859-640238	J051859.33-640238.7	49.1	80.5	4.6	-0.7
051415-645354	J051415.33-645354.0	9.0	19.4	4.9	-1.15
061501-684234	J061501.18-684234.0	32.3	50.9	5.5	-0.88
...	...	...	...	...	...

4.3 Spectral Index for the Entire Sample

CSS, GPS, Quasars and distant AGN cannot be distinguished easily by position in the sky in our catalogue as the angular resolutions of these existing radio surveys are, in most cases, insufficient. To remedy this, we have created a spectral index for each object to determine the dominant emission mechanism (see Table 3).

We perform a least squares linear fit to model the source's spectral index through the use of a power law consistent with the decay of synchrotron emission (a curved spectrum that would model synchrotron losses). However, fitting this simple single power-law model is not sufficient to categorise the turnover of GPS sources and other curved spectrum populations. Peacock (1985) showed that this type of analysis is only viable when applied to a small frequency range that ignores the effects of a curved spectrum.

As mentioned earlier, significant care must be taken when calculating the spectral index of a source. For instance, the resolution of each observation should be similar to avoid contributions from other sources. Initially, using all catalogues, we find a mean spectral index of −0.89 ±0.47 (and median of −0.92) from 3 789 sources that are detected at two or more radio frequencies (Table 8). We subse-

Table 8. Median and mean spectral index distributions for each subset in the catalogue for sources that are detected at more than one radio frequency.

Subset	Median α	Mean α	Standard Deviation	Number of Sources
All	−0.92	−0.89	0.47	3 789
Resolution Matched	−0.89	−0.88	0.48	3 636
rms Limited	−0.85	−0.81	0.45	2 984
AT20G Detection	−0.2	−0.21	0.44	41
No IR or optical	−0.95	−0.93	0.46	2 872
IR Counterpart	−0.84	−0.78	0.47	917
Optical Counterpart	−0.71	−0.66	0.49	209

Table 9. Source classification criteria for the radio continuum catalogue. † is unique sources detected at one or more frequencies.

Source Classification	Source Count	Classification Criteria	Catalogue Flag
All†	6 434		
Inverted α	146	$\alpha > 0$	
USS	546	$\alpha < -1.3$	USS
CSS	1 866	$-1.3 < \alpha < -0.8$	CSS
GPS	10	100 MHz < turnover < 5 GHz	GPS
HFP	14	SED peak above 5 GHz	HFP
IFRSs	67	various	IFRSs

quently refine this by presenting two spectral distributions; the first in Figure 6 (left), utilises all catalogues as presented in this paper. The second (and more accurate), Figure 6 (right) uses only the catalogues at 0.843 GHz and 1.384 GHz given their similar resolution as shown in Table 1. Consequently, we find a median spectral index of −0.89 and mean of −0.88 ±0.48 from 3 636 sources, summarised in Table 8. However, one should bear in mind that these spectral indices are measured between two close frequency values (0.843 and 1.384 GHz) which are affected by larger uncertainties. Indeed, some 50 sources (less than 1 per cent of the total population) in Table 3 have questionable spectral index estimates of $\alpha < -2$. Where the spectral index values are extreme, we flag those sources to emphasis caution. The reason for such unrealistic spectral indices for these few sources is that the flux density measurements are made between only two nearby frequency bands where a small change (or error) in size or flux density leads to large changes and somewhat unrealistic estimates in spectral index. Finally, looking at the median values of α in the last 3 lines of Table 8, one can see that the more distant the sources are (or the fewer optical/IR counterparts they have) the steeper their spectral index.

From this analysis, we find 1 866 (∼25 per cent) sources with an $\alpha < -0.8$ that we classify as CSS source candidates. Additionally we find 0 sources that have a highly inverted spectrum ($\alpha > 0.5$) that we classify as potential HFP sources in which the turnover is unconstrained due to our limited frequency range, as shown in Table 9.

We closely inspected the 41 AT20G sources in our catalogue (as shown in Figure 7), and found that the spectral index distribution of these sources is significantly different from the distribution for the catalogue as a whole (shown in Figures 6). This distribution has a mean α of −0.21 ±0.44 (Table 8). Among these 41 sources, we find 1 CSS, 0 GPS, 14 HFP and 0 Potential High Frequency Peaker (pHFP) sources which heavily skew the overall spectral index distribution towards $\alpha \sim 0$. This is due to a selection bias as we are selecting only sources with a detection in a shallower high frequency survey which tends to select bright sources with flat or inverted spectra. However, in practice we are biased towards FSRQ or BL Lacs.

Interestingly, sources that have an optical counterpart tend to have a flatter spectral index as shown in Figure 8 and summarised in Table 8. For example, we find the mean spectral index for this subsample to be −0.66 ±0.49 from 209 sources (Table 8). This is also reflected in radio sources that have an IR counterpart, but without an optical detection. Specifically, these sources have a mean spectral index of −0.78 ± 0.47 from 917 sources. In contrast, sources that do not have an IR or optical counterpart, have a far steeper mean spectral index at −0.93 ±0.46 from 2 872 sources (Table 8). As for the AT20G sample, this is probably a selection bias. These optical counterparts are mainly QSOs or BL Lacs with well-established flat spectral index. Similarly, but to a lesser extent, IR detected sources are more likely to have a strong IR AGN component, typical of a QSO and/or Seyfert 1 AGN, that tends to have flatter radio spectra. This interpretation seems supported by the fact that sources with no IR counterpart have steeper radio spectra on average, i.e. are more dominated by radio galaxies.

4.3.1 Sensitivity Limitations

Almost all sources (6 434 sources, 100 per cent) in our main catalogue (Table 3) are detected at 0.843 GHz or 1.384 GHz. The remaining 0 sources are weak sources detected in either the 4.8 or 8.64 GHz catalogues. These 0 sources may represent either variable sources or HFP (peaking their flux density above 5 GHz) as discussed in Sect. 4.3.3.

For a 5σ source to be included in the 1.384 GHz catalogue, an integrated flux density of at least 2.5 mJy is required (at the average rms noise of 0.5 mJy beam^{-1}). A 2.5 mJy source in the ATCA 1.384 GHz catalogue is expected to appear in the SUMSS catalogue only if it has a 0.843 GHz flux of 6 mJy (5 times the average rms), which would imply a very extreme spectral index of −1.7. For a more standard spectral index of −0.7 only sources with 1.384 GHz flux densities larger than 3.5 mJy can have a counterpart in the SUMSS catalogue.

This clearly limits the study of the spectral index of the 1.384 GHz source catalogue at the low flux density end, since 5–10σ 1.384 GHz sources might not be detected at 843 GHz due to the higher flux density limit of the SUMSS catalogue. It also introduces a bias in the study of the spectral index of the faintest 1.384 GHz sources, as only very steep sources can be detected at 0.843 GHz. This bias against flat-spectrum sources at the low (3–10σ) 1.384 GHz flux densities can be seen in Figure 9 (right panel), where we show the spectral index between 0.843 GHz and 1.384 GHz as a function of the integrated flux densities for the ATCA 1.384 GHz sources. The diagonal dashed line shows the limit of the region of the spectral index – flux parameter space where we can detect the source at both frequencies due to the limited sensitivity of the 0.843 GHz SUMSS catalogue. For sources above this line only spectral index limits can be derived. A similar bias can be in principle introduced when studying the spectral index of the SUMSS sources, this time against steep spectrum sources. Such a bias can however be neglected in our case, as the 1.384 GHz ATCA catalogue is more sensitive, and the faintest SUMSS sources (i.e. those detected at $5\sigma = 6$ mJy) can all have a counterpart in the 1.384 GHz ATCA catalogue, except for very extreme (and rare) cases where the spectral index is steeper than −1.7. Indeed, Figure 9 (left panel) shows that only a few SUMSS sources are not detected at 1.384 GHz (upper limits are shown as open grey squares at the bottom left).

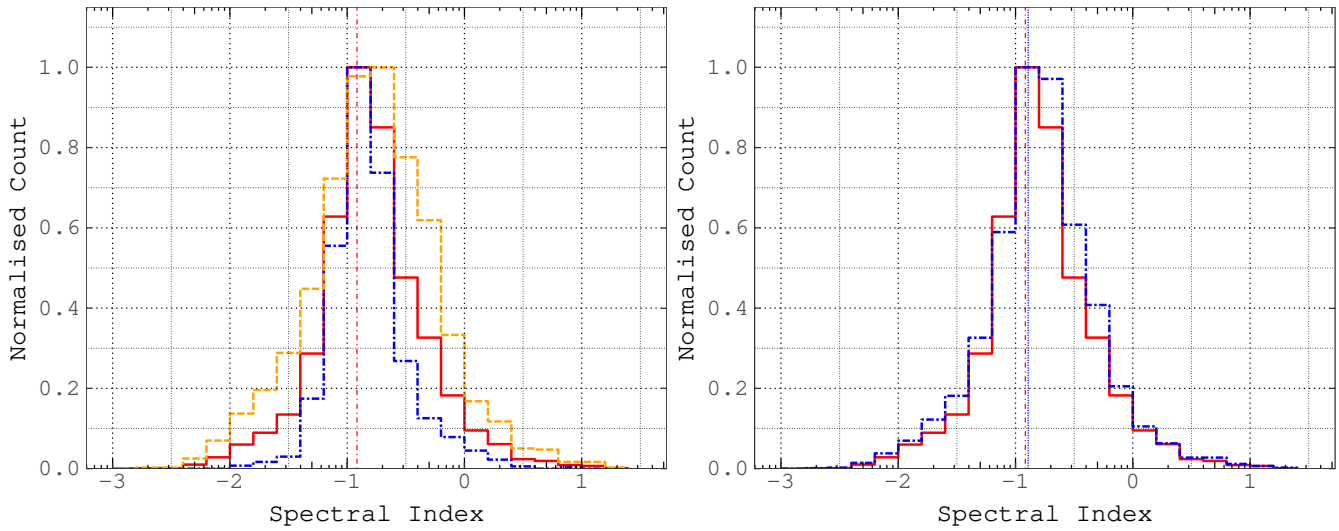

Figure 6. Left: Spectral index distribution for 3 789 sources from all radio continuum catalogues. The red continuous line is the full catalogue, the orange dashed line are spectral indices estimated from sources with only two available data points and blue dot-dashed line are estimates where more than two data points were available. The median α (vertical red dash-dotted line) for the full catalogue is −0.92 (Table 8). **Right:** A comparison between spectral index distributions for the full catalogue (red continuous line; same as in left figure) and for 3 636 spectral indices estimated from two data points between 0.843 GHz and 1.384 GHz (blue dot-dashed line). The spectral index measure is restricted to these two frequencies as they provide similar angular resolutions. The median α for the 0.843 GHz to 1.384 GHz two-point spectral indices (vertical blue dotted line) is −0.89 (Table 8). Counts per bin are normalised to the maximum count per bin in each sample.

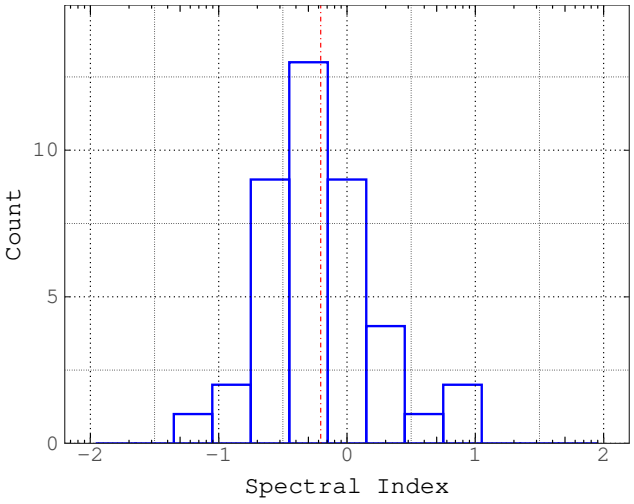

Figure 7. Spectral index distribution for 41 sources that have detection in the AT20G catalogue, measured using all radio continuum catalogues. The median α (vertical dash-dotted line) is −0.2.

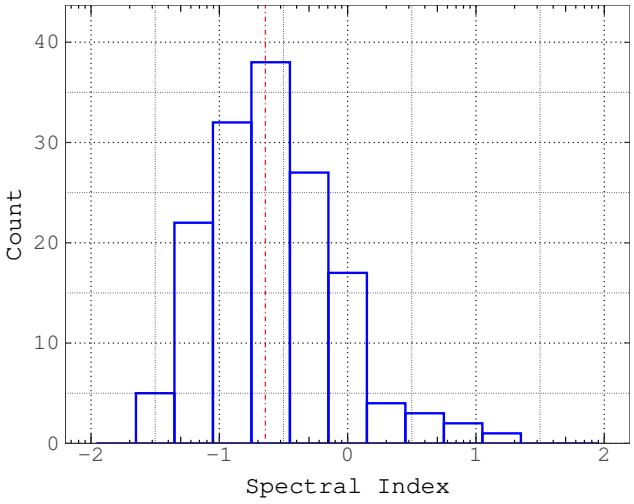

Figure 8. Spectral index distribution for 209 sources that have a detection in at least one optical catalogue, measured using all radio continuum catalogues. The median α (vertical dash-dotted line) is −0.71.

4.3.2 Spectral Flattening

Spectral flattening at low frequencies ($\leq$ 5 GHz) has been suggested in the literature, from studies of deep radio surveys. It is conjectured that the faint radio source populations of a few mJy have a flatter mean spectral index than brighter source populations. For instance Prandoni et al. (2006) studied the spectral index distribution of a sub-sample of sources extracted from the 1.4 and 5 GHz Australia Telescope ESO Slice Project (ATESP) surveys, finding a flatter mean (1.4 – 5 GHz) spectral index of –0.53±0.05 for sources with $S_{1.4\ \mathrm{GHz}} \leq 4$ mJy, when compared to –0.66±0.05 for sources above 4 mJy. These authors observed a similar behaviour for the 5 GHz selected sample, with mean spectral indices of –0.24±0.06 and –

Table 10. Spectral index statistics for the 1.384 GHz selected catalogue (ATCA), as derived in different flux density bins.

Lower (mJy)	Upper (mJy)	N	Median (α)	Mean (α)	σ_α
4.69	5.96	642	–0.51	–0.71	0.53
5.96	7.94	642	–0.67	–0.64	0.61
7.94	10.96	643	–0.77	–0.65	0.64
10.96	17.38	642	–0.81	–0.69	0.67
17.38	35.48	642	–0.83	–0.73	0.59
35.48	1548.82	643	–0.89	–0.79	0.75

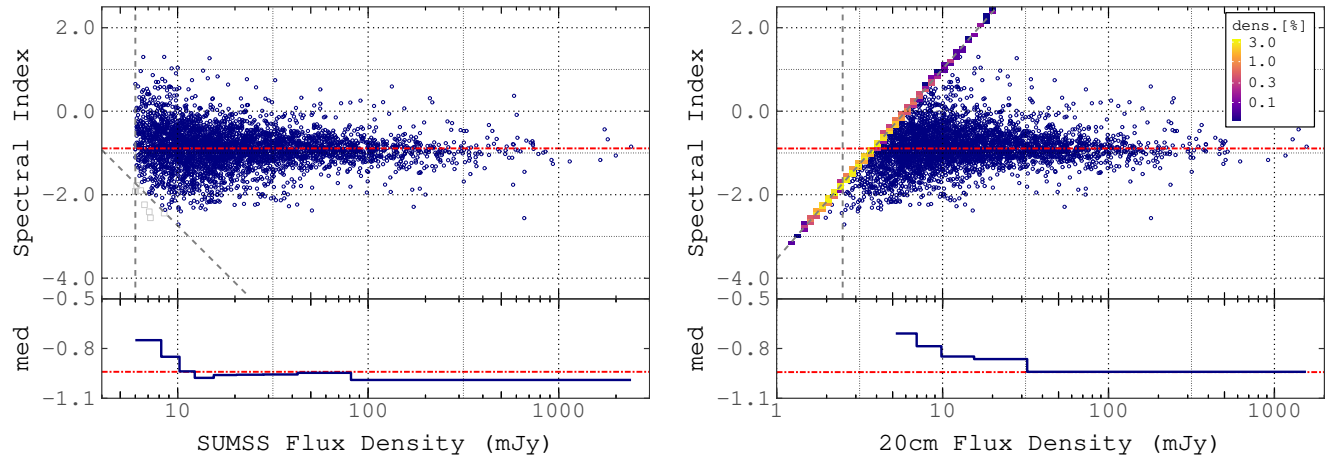

Figure 9. Integrated flux density vs. spectral index for the two most complete survey lists: SUMSS (left) and ATCA at 1.384 GHz (**top panels**) and the distribution of spectral index medians per flux density bin (**bottom panels**). Vertical dashed lines in top panels indicate flux limits for each survey. Red horizontal dot-dashed lines in all panels represent the median spectral index (−0.89) for the complete sample of all sources in common to SUMSS and ATCA surveys. For the ATCA 1.384 GHz data points with no counterparts at 0.843 GHz we show the approximate source counts (in %) of the limiting spectral indices as a binned density map (scale bar shown at the top right corner). For the median vs flux density plots data is split in 9 equally populated bins. Note that the bins with more points from limiting than calculated spectral indices are not shown.

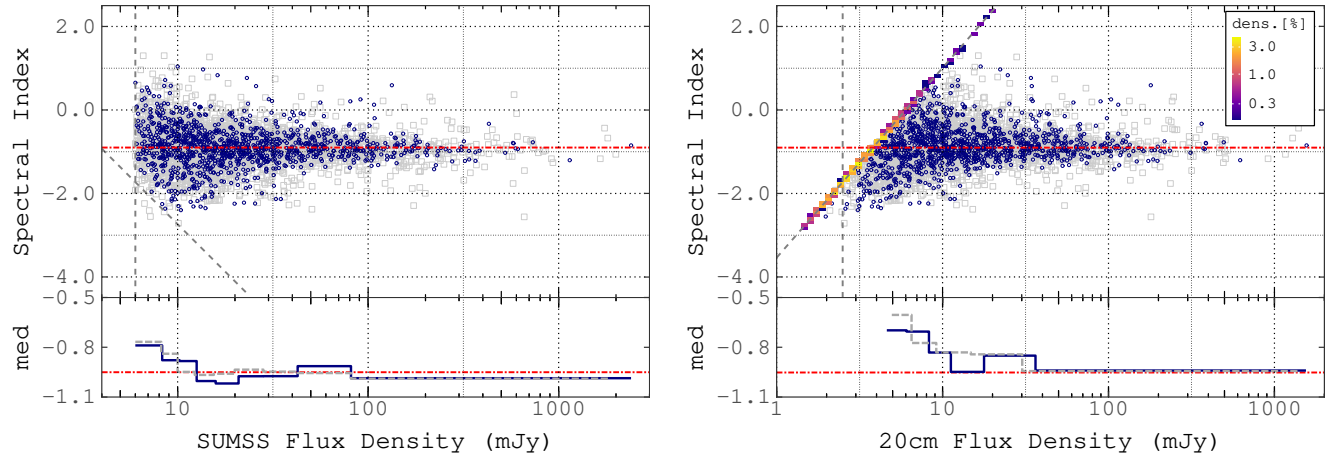

Figure 10. As in Figure 9 but splitting the sample into two groups: Open circles represent sources within 3.5° from the LMC centre (*inner* subsample) while open squares are sources outside this radius (*outer* subsample). In the bottom panels we show the distribution of spectral index medians per, equally populated, flux density bin for the *inner* subsample (blue solid line) and *outer* subsample (gray dashed line) separately. No significant difference in source spectral index distribution is observed between the two groups, indicating that our catalogue is mainly comprised of background sources.

Table 11. Spectral index statistics for the 0.843-GHz selected catalogue (SUMSS), as derived in different flux density bins.

Lower (mJy)	Upper (mJy)	N	Median (α)	Mean (α)	σ_α
6.00	8.00	373	–.68	–0.67	0.57
8.00	9.79	369	–0.79	–0.79	0.61
9.79	11.75	359	–0.89	–0.90	0.53
11.75	14.45	362	–0.89	–0.94	0.53
14.45	17.78	357	–0.95	–0.97	0.49
17.78	22.91	360	–0.89	–0.89	0.43
22.91	31.62	363	–0.92	–0.92	0.42
31.62	47.86	361	–0.91	–0.92	0.38
47.86	89.13	361	–0.90	–0.87	0.31
89.13	2398.83	363	–0.95	–0.95	0.35

0.58±0.06 respectively below and above 4 mJy, in line with previous results based on smaller samples (Donnelly et al. 1987; Fomalont et al. 1991). The flatter values at 5 GHz were expected as higher frequency surveys tend to select source populations with flatter spectra. More recently Owen et al. (2009) pushed the spectral index analysis to lower flux densities ($S_{1.4\,GHz} > 10$ μJy) and lower frequencies (0.330 MHz), finding similar results: in the SWIRE deep field they measured median (0.33 – 1.4 GHz) spectral indices of –0.54±0.06 in the flux interval $S_{1.4\,GHz} \sim 0.3 - 1$ mJy, and –0.66±0.11 at larger flux densities. Both Prandoni et al. (2006) and Owen et al. (2009) found that this flattening is mostly associated with compact sources, likely core dominated AGN. Interestingly Owen et al. (2009) find a significant re-steepening at $S_{1.4\,GHz} < 0.3$ mJy, which is interpreted as the result of star forming galaxies becoming the dominant population in the μJy regime.

It should be noted, however, that the tendency of radio source spectra to become flatter with decreasing flux density is not observed by all authors. For instance, Randall et al. (2012) and Zinn et al. (2012) found no statistical spectral flattening for mJy sources.

This however could be a consequence of not well-matched sensitivities at the various frequencies, which might prevent the spectral index analysis to be applied to the faintest sources, as discussed in Sect. 4.3.1. Indeed, the 1.4 GHz survey by Zinn et al. (2012) has a rms ~3 times lower than that of their 2.3 GHz survey.

In order to provide further clues on this matter, we searched for spectral index – flux density trends in our LMC field catalogue. Tables 10 and 11 show the mean and median values of the spectral index as a function of 1.384 and 0.843 GHz flux densities respectively. The median values are also shown in the bottom panels of Figure 9. As discussed in Sect. 4.3.1, the limited sensitivity of the 0.843 GHz catalogue makes it unreliable for any spectral index analysis of the faintest 1.384 GHz selected sources, as only very steep-spectrum sources can be detected at both frequencies and spectral index limits become dominant. For this reason, we decided to restrict our analysis of the 1.384 GHz ATCA sample to flux densities where spectral index limits represent less than 50 per cent of the total number of sources in the flux bin under consideration, allowing us to get reliable median spectral index values. This happens at $S_{1.4\ GHz} > 4.7$ mJy. For the shallower SUMSS catalogue, we do not have significant biases and the analysis can be pushed down to the catalogue flux limit (i.e. 6 mJy).

We notice that the spectral flattening reported in previous works is observed at lower flux densities than those probed by the present study. Nevertheless, the larger statistics available allows us to split our sources in finer flux density bins. This in turn allows us to identify a small but clear trend towards flatter spectral indices already at S<10 mJy. We also notice that median spectral index values tend to be flatter for sources in the 1.384 GHz catalogue than for those in the 0.843 GHz catalogue, consistent with the results of Prandoni et al. (2006), where flatter spectral index values were found for the higher frequency selected sample.

Focusing on the 1.384 GHz catalogue, where spectral index values can be directly examined, we find that a median[5] spectral index value of –0.51 at S~5 mJy is consistent with the –0.53 found by Prandoni et al. (2006) at S<4 mJy and the –0.54 found by Owen et al. (2009) at S<1 mJy, indicating we may be probing the same radio source population. Also, consistent with the mean values measured at higher fluxes: they vary from –0.64 to –0.69 in the flux range 6–17 mJy, against a value of –0.66 reported by Prandoni et al. (2006) at S>4 mJy.

In order to test if there is any difference in spectral index distribution (including a possible contribution to the source spectral flattening) of sources belonging to the LMC, we constructed the same graphs for the sources inside of the 3.5° radius from the approximate centroid of the LMC at RA = 79.5 deg and Dec = −68.9 deg (Figure 10). We found no difference in source spectral index distribution within or outside the 3.5° radius (filled circles and open squares respectively), indicating that our catalogue is mainly comprised of background sources.

4.3.3 *Radio Two-Colour Diagram*

We adopt the radio "two-colour" diagram as shown by Sadler et al. (2006) in order to allow the identification of sources with curved spectra (Figure 12). This approach treats the high and low frequency components of each source separately, by calculating two spectral indices. Here, we define our high frequency sample as >1.5 GHz and our low frequency sample as the inverse case (i.e. <1.5 GHz). This analysis should be treated with caution as the spectral index was calculated based on flux densities from observations with different angular resolutions.

Using the radio two-colour diagram, we find 10 sources with a spectral index of $\alpha^{20\ GHz}_{1.5\ GHz} \leq 0 \leq \alpha^{1.5\ GHz}_{0.2\ GHz}$. This limited sample is primarily due to the lower source density at 20 GHz.

We used a 2nd order polynomial to determine the turnover frequency for GPS candidates. In Figure 11 we show an example of radio spectra of one of the objects from this sample fitted with 2nd order polynomial.

With these estimated turnover frequencies, we use Equation 2 to determine the Largest Linear Size (LLS) for each GPS candidate, as shown in Table 12. The average turnover frequency for this sample of GPS sources is 1.73 GHz with a corresponding average LLS of 320 pc. These results are consistent with findings of Jeyakumar (2016).

We find 14 sources that have a convex spectrum with a peaked (turnover) integrated flux density above 5 GHz and, as such, we follow Dallacasa et al. (2000) classification and label them as HFP sources.

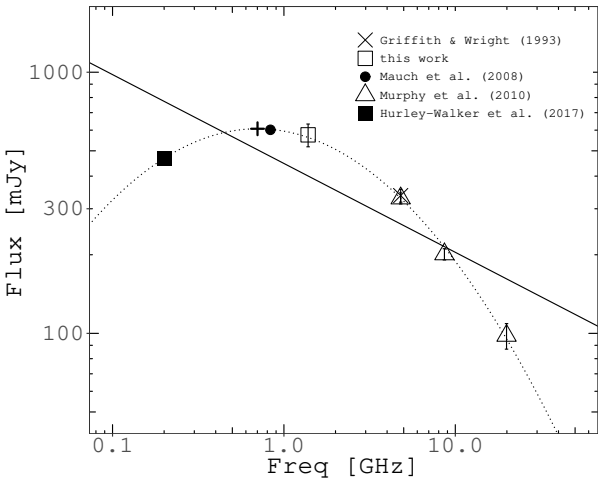

Figure 11. Example of the radio spectra of one of the GPS candidates (J061011–724814) fitted with a 2nd order polynomial (dotted line) and power-law function (continuous line). A cross (+) represents the location of the estimated turnover frequency.

Table 12. Turnover frequency and linear size relation (using equation 2) for our sample of GPS candidate sources.

Source Name	Turnover ν (GHz)	LLS (kpc)	Candidate Type
045358-713817	2.05	0.16	GPS
045516-705446	2.71	0.10	GPS
050000-632237	1.00	0.47	GPS
050139-662525	1.05	0.44	GPS
052310-720624	1.76	0.20	GPS
052505-664052	2.29	0.13	GPS
052517-672246	1.62	0.23	GPS
054317-662655	3.14	0.08	GPS
054736-680905	0.94	0.52	GPS
061011-724813	0.70	0.82	GPS

[5] The mean spectral index value in this flux bin is not well constrained due to the many spectral index limits.

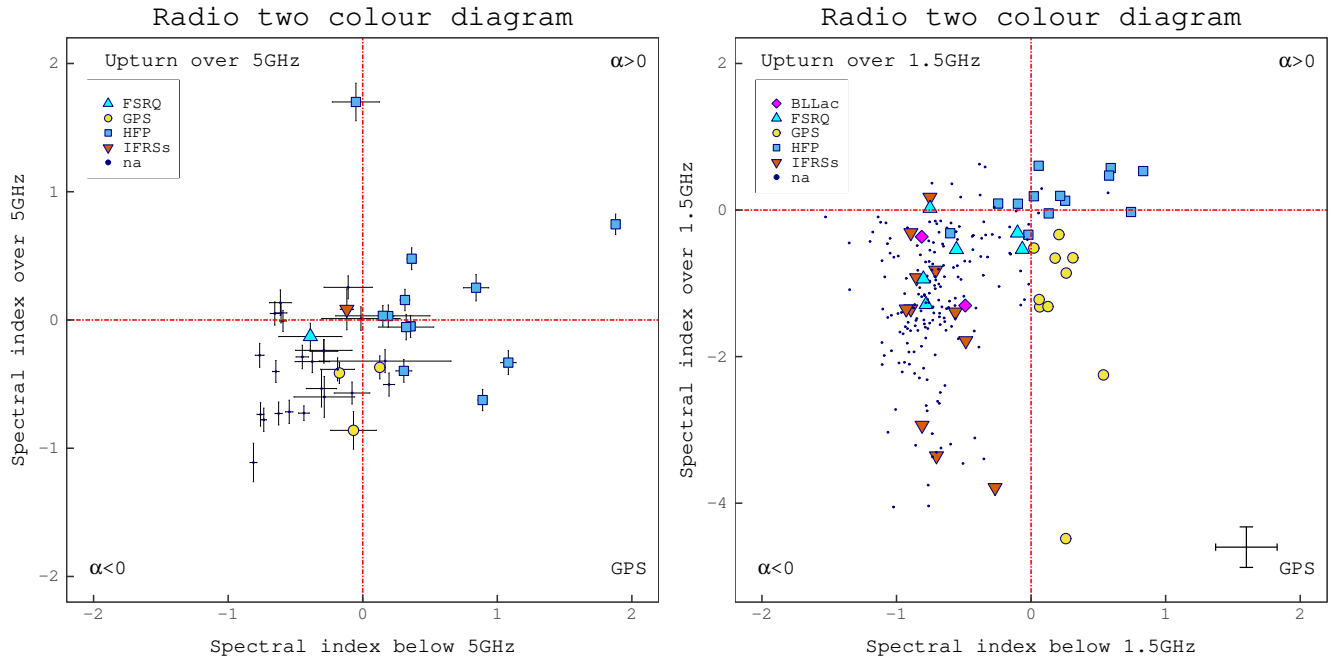

Figure 12. 5 GHz radio "two-colour" diagram (left) for 41 sources, contrasting two spectral index measurements for each source divided at 5 GHz. The median α for the low frequency measurement is −0.17 and the mean α for the high frequency measurement is −0.29. 1.5 GHz radio two-colour diagram (right) for 234 sources, contrasting two spectral index measurements for each source divided at 1.5 GHz. The median α for the low frequency measurement is −0.71 and the mean α for the high frequency measurement is −1.04. In the lower right corner we show median errors in estimated spectral indices. In the upper left corner (both plots) we show the colour code of the points for different classes presented here.

5 SUMMARY AND CONCLUSION

We have compiled a master catalogue based on several new and existing radio continuum lists of sources behind the LMC, to a 5σ detection level from ~200 mJy down to 0.2 mJy, depending on observing frequency (see Table 1). From this, a total of 6 434 sources have been identified, with multi-frequency detections of 3 789 sources. We find the median spectral index of $\alpha = -0.89$ for 3 636 sources which are detected at two frequencies (0.843 and 1.384 GHz) with similar resolution (FWHM ~40–45 arcsec). We have cross-matched these 6 434 sources with and five optical surveys (see Table 2). As a result, we find optical counterparts for 343, of which 128 have a redshift measurement with a mean redshift of 0.39.

Based on the SUMSS and 1.384 GHz ATCA source lists, we present evidence that radio sources below 10 mJy exhibit flatter radio spectra than brighter ones. To take into account the biases introduced by the limited sensitivity of the 0.843 GHz SUMSS catalogue, we restricted our analysis to 1.384 GHz flux densities S> 5 mJy. As a result, we obtain median (0.843–1.384 GHz) spectral indices flattening from values of < -0.8 for $S_{1.4\ \mathrm{GHz}} > 10$ mJy to –0.51 for $S_{1.4\ \mathrm{GHz}} < 5$ mJy. This is in general agreement with findings from previous deep surveys (Prandoni et al. 2006; Owen et al. 2009).

Additionally, 1 866 unresolved sources have been detected with a spectral index of < -0.8 between 408 MHz and 20 GHz (Sect. 4.2.1). This is a strong indicator for young AGN that are either CSS or GPS objects. Furthermore we find evidence for 10 of these sources to be GPS candidates, that have $\alpha^{20\ \mathrm{GHz}}_{5\ \mathrm{GHz}} \leq 0 \leq \alpha^{5\ \mathrm{GHz}}_{843\ \mathrm{MHz}}$. We classify 14 sources as HFP and 0 as possible HFP sources (see Table 9) that have steep inverted spectra where we do not observe a turnover (i.e. the turnover frequency is > 20 GHz).

6 DATA AVAILABILITY

The catalogues underlying this article will be made available on the CDS[6] website when the paper is published.

ACKNOWLEDGEMENTS

The Australian SKA Pathfinder is part of the Australia Telescope National Facility which is managed by Australian Commonwealth Scientific and Industrial Research Organisation (CSIRO). Operation of ASKAP is funded by the Australian Government with support from the National Collaborative Research Infrastructure Strategy. ASKAP uses the resources of the Pawsey Supercomputing Centre. Establishment of ASKAP, the Murchison Radio-astronomy Observatory and the Pawsey Supercomputing Centre are initiatives of the Australian Government, with support from the Government of Western Australia and the Science and Industry Endowment Fund. We acknowledge the Wajarri Yamatji people as the traditional owners of the Observatory site. This work was supported by resources provided by the Pawsey Supercomputing Centre with funding from the Australian Government and the Government of Western Australia. This paper includes archived data obtained through the Australia Telescope Online Archive (http://atoa.atnf.csiro.au). The Australia Telescope Compact Array is part of the Australia Telescope National Facility which is funded by the Australian Government for operation as a National Facility managed by CSIRO. Parts of this research were conducted with the support of Australian Research Council Centre of Excellence for AllSky Astrophysics in 3 Dimensions (ASTRO 3D), through project number CE170100013.

[6] https://cds.u-strasbg.fr/

IP acknowledges support from INAF under the SKA/CTA PRIN "FORECaST" and the PRIN MAIN STREAM "SAuROS" projects. H.A. has benefited from grant CIIC 174/2021 of Universidad de Guanajuato, Mexico. D.U. acknowledges Ministry of Education, Science and Technological Development of the Republic of Serbia through the contract No. 4451-03-9/2021-14/200104.

REFERENCES

Alexander P., 2000, MNRAS, 319, 8
An T., Baan W. A., 2012, ApJ, 760, 77
Antonucci R., 1993, ARA&A, 31, 473
Bock D. C.-J., Large M. I., Sadler E. M., 1999, AJ, 117, 1578
Bozzetto L. M., et al., 2017, ApJS, 230, 2
Callingham J. R., et al., 2017, ApJ, 836, 174
Collier J. D., et al., 2014, MNRAS, 439, 545
Collier J. D., et al., 2018, MNRAS, 477, 578
Condon J. J., Cotton W. D., Greisen E. W., Yin Q. F., Perley R. A., Taylor G. B., Broderick J. J., 2002, VizieR Online Data Catalog, 8065, 0
Dallacasa D., Orienti M., 2016, Astronomische Nachrichten, 337, 120
Dallacasa D., Stanghellini C., Centonza M., Fanti R., 2000, A&A, 363, 887
De Zotti G., Granato G. L., Silva L., Maino D., Danese L., 2000, A&A, 354, 467
Dickel H. R., 2000, Baltic Astronomy, 9, 564
Dickel J. R., McIntyre V. J., Gruendl R. A., Milne D. K., 2005, AJ, 129, 790
Donnelly R. H., Partridge R. B., Windhorst R. A., 1987, ApJ, 321, 94
Fanti C., 2009, Astronomische Nachrichten, 330, 120
Fanti C., Fanti R., Dallacasa D., Schilizzi R. T., Spencer R. E., Stanghellini C., 1995, A&A, 302, 317
Filipovic M. D., Haynes R. F., White G. L., Jones P. A., Klein U., Wielebinski R., 1995, A&AS, 111, 311
Filipovic M. D., White G. L., Jones P. A., Haynes R. F., Pietsch W. N., Wielebinski R., Klein U., 1996a, in Burkert A., Hartmann D. H., Majewski S. A., eds, Astronomical Society of the Pacific Conference Series Vol. 112, The History of the Milky Way and Its Satellite System. p. 91
Filipovic M. D., White G. L., Haynes R. F., Jones P. A., Meinert D., Wielebinski R., Klein U., 1996b, A&AS, 120, 77
Filipovic M. D., Jones P. A., White G. L., Haynes R. F., 1998a, Publ. Astron. Soc. Australia, 15, 128
Filipovic M. D., Haynes R. F., White G. L., Jones P. A., 1998b, A&AS, 130, 421
Filipovic M. D., Jones P. A., White G. L., Haynes R. F., 1998c, A&AS, 130, 441
Filipović M. D., et al., 2009, MNRAS, 399, 769
Fomalont E. B., Windhorst R. A., Kristian J. A., Kellerman K. I., 1991, AJ, 102, 1258
For B.-Q., et al., 2018, MNRAS, 480, 2743
Gaensler B. M., Haverkorn M., Staveley-Smith L., Dickey J. M., McClure-Griffiths N. M., Dickel J. R., Wolleben M., 2005, Science, 307, 1610
Galvin T. J., et al., 2018, MNRAS, 474, 779
Gregory P. C., Condon J. J., 1991, ApJS, 75, 1011
Griffith M. R., Wright A. E., 1993, AJ, 105, 1666
Haberl F., 2019, in A Synoptic View of the Magellanic Clouds: VMC, Gaia and Beyond. p. 63, doi:10.5281/zenodo.3472583
Hancock P. J., Murphy T., Gaensler B. M., Hopkins A., Curran J. R., 2012a, Aegean: Compact source finding in radio images, Astrophysics Source Code Library (ascl:1212.009)
Hancock P. J., Murphy T., Gaensler B. M., Hopkins A., Curran J. R., 2012b, MNRAS, 422, 1812
Hancock P. J., Trott C. M., Hurley-Walker N., 2018, Publ. Astron. Soc. Australia, 35, e011
Harvey-Smith L., Hardwick J. A., De Marco O., Parthasarathy M., Gonidakis I., Akhter S., Cunningham M., Green J. A., 2018, MNRAS, 479, 1842
Haynes R. F., et al., 1991, A&A, 252, 475
Heywood I., et al., 2016, MNRAS, 457, 4160
Hilditch R. W., Howarth I. D., Harries T. J., 2005, MNRAS, 357, 304
Hopkins A. M., et al., 2015, Publ. Astron. Soc. Australia, 32, e037
Hotan A. W., et al., 2014, Publ. Astron. Soc. Australia, 31, e041
Hughes A., Wong T., Ekers R., Staveley-Smith L., Filipovic M., Maddison S., Fukui Y., Mizuno N., 2006, MNRAS, 370, 363
Hughes A., Staveley-Smith L., Kim S., Wolleben M., Filipović M., 2007, MNRAS, 382, 543
Hurley-Walker N., et al., 2017, MNRAS, 464, 1146
Jarrett T. H., Chester T., Cutri R., Schneider S., Skrutskie M., Huchra J. P., 2000, AJ, 119, 2498
Jarvis M. J., Teimourian H., Simpson C., Smith D. J., Rawlings S., Bonfield D., 2009, Monthly Notices of the Royal Astronomical Society: Letters, 398, L83
Jeyakumar S., 2016, MNRAS, 458, 3786
Jones D. H., Saunders W., Read M., Colless M., 2005a, Publ. Astron. Soc. Australia, 22, 277
Jones H., Saunders W., Colless M., Read M., Parker Q., Watson F., Campbell L., 2005b, in Fairall A. P., Woudt P. A., eds, Astronomical Society of the Pacific Conference Series Vol. 329, Nearby Large-Scale Structures and the Zone of Avoidance. p. 11
Jones D. H., et al., 2009, MNRAS, 399, 683
Joye W. A., Mandel E., 2003, in Payne H. E., Jedrzejewski R. I., Hook R. N., eds, Astronomical Society of the Pacific Conference Series Vol. 295, Astronomical Data Analysis Software and Systems XII. p. 489
Kaczmarek J. F., Purcell C. R., Gaensler B. M., McClure-Griffiths N. M., Stevens J., 2017, MNRAS, 467, 1776
Kauffmann G., et al., 2003, MNRAS, 346, 1055
Kazanas D., Fukumura K., Behar E., Contopoulos I., Shrader C., 2012, The Astronomical Review, 7, 92
Kim D.-W., Protopapas P., Trichas M., Rowan-Robinson M., Khardon R., Alcock C., Byun Y.-I., 2012, ApJ, 747, 107
Kozłowski S., Kochanek C. S., 2009, ApJ, 701, 508
Kozłowski S., Kochanek C. S., Udalski A., 2011, ApJS, 194, 22
Kozłowski S., et al., 2012, ApJ, 746, 27
Kozłowski S., et al., 2013, ApJ, 775, 92
Large M. I., Mills B. Y., Little A. G., Crawford D. F., Sutton J. M., 1981, MNRAS, 194, 693
Leahy D., Wang Y., Lawton B., Ranasinghe S., Filipović M., 2019, AJ, 158, 149
Leverenz H., Filipović M. D., Vukotić B., Urošević D., Grieve K., 2017, MNRAS, 468, 1794
Line J. L. B., Webster R. L., Pindor B., Mitchell D. A., Trott C. M., 2017, Publ. Astron. Soc. Australia, 34, e003
Lonsdale C. J., et al., 2016, Astronomische Nachrichten, 337, 194
Maggi P., et al., 2016, A&A, 585, A162
Maggi P., et al., 2019, A&A, 631, A127
Mao S. A., et al., 2012, ApJ, 759, 25
Marecki A., Spencer R. E., Kunert M., 2003, Publ. Astron. Soc. Australia, 20, 46
Marocco F., et al., 2021, ApJS, 253, 8
Mathewson D. S., Cleary M. N., Murray J. D., 1974, ApJ, 190, 291
Mauch T., Murphy T., Buttery H. J., Curran J., Hunstead R. W., Piestrzynski B., Robertson J. G., Sadler E. M., 2003, MNRAS, 342, 1117
Mauch T., Murphy T., Buttery H. J., Curran J., Hunstead R. W., Piestrzynski B., Ropbertson J. G., Sadler E. M., 2008, VizieR Online Data Catalog, 8081, 0
Meixner M., et al., 2006, AJ, 132, 2268
Middelberg E., et al., 2008, AJ, 135, 1276
Mills B. Y., Turtle A. J., 1984, in van den Bergh S., de Boer K. S. D., eds, IAU Symposium Vol. 108, Structure and Evolution of the Magellanic Clouds. pp 283–290
Murphy T., et al., 2010, MNRAS, 402, 2403
Norris R. P., et al., 2006, AJ, 132, 2409
O'Dea C. P., 1998, PASP, 110, 493
O'Dea C. P., Baum S. A., 1997, AJ, 113, 148
O'Dea C. P., Saikia D. J., 2021, A&ARv, 29, 3
Ochsenbein F., Bauer P., Marcout J., 2000, A&AS, 143, 23
Orenstein B. J., Collier J. D., Norris R. P., 2019, MNRAS, 484, 1021
Orienti M., Dallacasa D., 2008, A&A, 477, 807

Orienti M., Dallacasa D., 2014, MNRAS, 438, 463
Owen F. N., Morrison G. E., Klimek M. D., Greisen E. W., 2009, AJ, 137, 4846
Parker Q. A., Bojičić I. S., Frew D. J., 2016, in Journal of Physics Conference Series. p. 032008 (arXiv:1603.07042)
Payne J. L., Filipovic M. D., Millar W. C., Crawford E. J., de Horta A. Y., Stootman F. H., Urosevic D., 2008, Serbian Astronomical Journal, 177, 53
Payne J. L., Tauber L. A., Filipovic M. D., Crawford E. J., de Horta A. Y., 2009, Serbian Astronomical Journal, 178, 65
Peacock J. A., 1985, MNRAS, 217, 601
Pennock C. M., et al., 2021, arXiv e-prints, p. arXiv:2106.12013
Pietrzyński G., et al., 2013, Nature, 495, 76
Pietrzyński G., et al., 2019, Nature, 567, 200
Polatidis A. G., Conway J. E., 2003, Publ. Astron. Soc. Australia, 20, 69
Prandoni I., Parma P., Wieringa M. H., de Ruiter H. R., Gregorini L., Mignano A., Vettolani G., Ekers R. D., 2006, A&A, 457, 517
Randall K. E., Hopkins A. M., Norris R. P., Edwards P. G., 2011, MNRAS, 416, 1135
Randall K. E., Hopkins A. M., Norris R. P., Zinn P.-C., Middelberg E., Mao M. Y., Sharp R. G., 2012, MNRAS, 421, 1644
Readhead A. C. S., Taylor G. B., Pearson T. J., Wilkinson P. N., 1996, ApJ, 460, 634
Reid W. A., 2014, MNRAS, 438, 2642
Reid W. A., Parker Q. A., 2013, MNRAS, 436, 604
Reynolds J., 1994, ATNF Technical Memos, 39.3 040, available at: http://www.atnf.csiro.au/observers/memos/d96783~1.pdf
Riess A. G., Casertano S., Yuan W., Macri L. M., Scolnic D., 2019, ApJ, 876, 85
Sadler E. M., et al., 2006, MNRAS, 371, 898
Saxena A., et al., 2018, MNRAS, 480, 2733
Skrutskie M. F., et al., 2006, AJ, 131, 1163
Smith R. C., MCELS Team 1998, Publ. Astron. Soc. Australia, 15, 163
Taylor M. B., 2005, in Shopbell P., Britton M., Ebert R., eds, Astronomical Society of the Pacific Conference Series Vol. 347, Astronomical Data Analysis Software and Systems XIV. p. 29
Taylor M., 2011, TOPCAT: Tool for OPerations on Catalogues And Tables, Astrophysics Source Code Library (ascl:1101.010)
Udalski A., et al., 1994, Acta Astron., 44, 165
Urry M., 2003, in Collin S., Combes F., Shlosman I., eds, Astronomical Society of the Pacific Conference Series Vol. 290, Active Galactic Nuclei: From Central Engine to Host Galaxy. p. 3 (arXiv:astro-ph/0301309)
Urry C. M., Padovani P., 1995, PASP, 107, 803
Viechtbauer W., 2010, Journal of Statistical Software, 36, 1
Vukotić B., Urošević D., Filipović M. D., Payne J. L., 2009, A&A, 503, 855
Waddington I., Windhorst R. A., Cohen S. H., Partridge R. B., Spinrad H., Stern D., 1999, ApJ, 526, L77
Wayth R. B., et al., 2015, Publ. Astron. Soc. Australia, 32, e025
Wenger M., et al., 2000, A&AS, 143, 9
Wright E. L., et al., 2010, AJ, 140, 1868
Yamashita T., et al., 2020, AJ, 160, 60
Yew M., et al., 2021, MNRAS, 500, 2336
Zinn P. C., Middelberg E., Ibar E., 2011, A&A, 531, A14
Zinn P.-C., Middelberg E., Norris R. P., Hales C. A., Mao M. Y., Randall K. E., 2012, A&A, 544, A38
Żywucka N., Goyal A., Jamrozy M., Stawarz Ł., Ostrowski M., Kozłowski S., Udalski A., 2018, ApJ, 867, 131

This paper has been typeset from a TEX/LATEX file prepared by the author.